Engineering Failure Analysis 175 (2025) 109578

Contents lists available at ScienceDirect

Engineering Failure Analysis

journal homepage: www.elsevier.com/locate/engfailanal

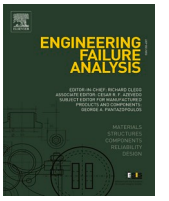

Predicting the fracture initiation of dual-phase steels under different stress paths through an implicit stress update scheme☆

Toros Arda Akşen [a,*], Neslihan Özsoy [a], Emre Esener [b], Murat Özsoy [a], Mehmet Fırat [a]

[a] Sakarya University, Mechanical Engineering Department, 54050 Sakarya, Turkiye
[b] Bilecik Seyh Edebali University, Mechanical Engineering Department, 11100 Bilecik, Turkiye

ARTICLE INFO

Keywords:
Anisotropic plasticity modeling
Ductile fracture
Dual-Phase steels
Finite element analysis
Nakajima test

ABSTRACT

Dual-phase steels are extensively utilized materials in automotive parts to reduce the weight of the autobody and increase fuel performance. Since most of the parts in the autobody are subjected to different loading conditions, the fracture initiation limits of these steels have become significant in recent years. This study systematically investigates the effects of anisotropic plasticity modeling on the ductile fracture predictions and forming limit curves (FFLCs) of dual-phase steels (DP600 and DP800), commonly utilized in automotive applications. Experimental uniaxial tensile tests were performed in multiple material orientations to characterize anisotropic mechanical responses, and these data were used to calibrate the sixth-order polynomial-based anisotropic yield criterion (HomPol6). Additionally, tensile tests on four notched geometries were conducted to provide stress state-dependent fracture strains, facilitating calibration of the DF2016 ductile fracture model. Notably, the calibration procedures were separately conducted for isotropic (von Mises) and anisotropic (HomPol6) yield criteria to critically evaluate their effects on fracture prediction accuracy. A detailed theoretical discussion is provided regarding the discrepancies observed in equivalent plastic strain, stress triaxiality, and Lode parameters between isotropic and anisotropic constitutive models, highlighting the intrinsic dependence of stress state evolution on anisotropic plastic flow. Subsequently, Finite Element (FE) analyses of the Nakajima tests were implemented using an implicit Marc solver with user-defined material subroutines (Hypela2). The numerical FFLC predictions obtained using the anisotropic calibration demonstrated enhanced agreement with experimentally derived literature data compared to the isotropic approach, explicitly highlighting the importance of anisotropic constitutive modeling. Furthermore, this study elucidates how critical numerical factors, such as friction, contact mechanics, mesh discretization, and bending effects in the Nakajima tests, interact with anisotropy to influence FFLC predictions. Finally, clear recommendations are provided for future experimental and theoretical directions, emphasizing the necessity of developing fully anisotropic fracture criteria to comprehensively capture orientation-dependent fracture ductility in advanced high-strength steels.

☆ This article is part of a special issue entitled: 'ICEFAX' published in Engineering Failure Analysis.

* Corresponding author.
E-mail addresses: ardaaksen@sakarya.edu.tr (T.A. Akşen), nerken@sakarya.edu.tr (N. Özsoy), emre.esener@bilecik.edu.tr (E. Esener), ozsoy@sakarya.edu.tr (M. Özsoy), firat@sakarya.edu.tr (M. Fırat).

https://doi.org/10.1016/j.engfailanal.2025.109578
Received 21 October 2024; Received in revised form 2 April 2025; Accepted 2 April 2025
Available online 5 April 2025

1. Introduction

The competition in the automotive industry, coupled with the European Commission regulations for reducing greenhouse and CO_2 emissions, yields new attempts to develop advanced materials to reduce the automobile's weight and compensate for the strength for ensuring crashworthiness. Advanced high-strength steels are the essential solutions in this regard, and among them, the dual-phase (DP) steels are employed prevalently owing to their excellent ferrite-martensite combination-based microstructure [1–3]. The heterogeneity of the microstructure ensures enhanced formability characteristics. Hence, fracture initiation features, especially for different stress state conditions in DP steels, became essential data in the automotive industry [4–7]. The fracture forming limit curve (FFLC) is essential for acquiring information about fracture initiation in different loading conditions. However, experimental acquisition of FFLC is generally provided by the Nakajima test, in which several specimens with different web widths were stretched through a punch, and this test leads to considerable cost. On the other hand, the FFLC data can be obtained by analytical and numerical approaches as well [8–12]. Although these approaches surmount the financial issues, knowledge of the combination of plasticity, ductile fracture, calibration, and optimization has been indispensable.

Computer science and software advances facilitate intricate numerical computations; nonetheless, computational approaches, such as Finite Element (FE) analyses, also necessitate the validation of numerical results to ensure their reliability. The FE solvers adopt implicit or explicit methodologies for computing the field variables, such as stress and strain data [13]. Although there are specific differences between the implicit and explicit methodologies, plasticity modeling is one of the distinct issues. The explicit solvers regard the data from the previous domain' while the implicit solvers consider the current domain so as to fulfil the requirements of the yield condition. Further, the implicit solvers employ the return mapping scheme to satisfy the consistency condition and surmount the so-called yield surface drifting issue encountered in explicit methodology [14,15]. However, the implicit solvers require a high computational cost that complicates the implementation of the constitutive modeling.

The FE method includes numerical factors such as mesh discretizing, element type, friction, contact algorithm, etc. Moreover, for the processes such as the Nakajima test, the sheet is bent by a punch that induces biaxial tension on the reverse side of the sheet. This situation also leads to deviations in the loading path [16–18]. All these factors influence the prediction of fracture initiation and may not be regarded by the analytical approaches. On the other hand, plasticity modeling is crucial for both analytical and numerical approaches. The yield criterion definition is one of the essential stages of plasticity modeling, and the sheet's anisotropy is directly relevant to the yield criterion [19,20]. Hill48 yield criterion is the initial anisotropic yield criterion that is also viable today for steel sheets [21,22]. However, the employment of most of the anisotropic yield criteria introduced in the past was restricted because they failed to characterize the anisotropic response for highly textured sheets and could not construct the completely convex yield locus [23–25]. However, the recently introduced enhanced yield criteria, such as linear transformation-based [26,27] and polynomial-based [28], can prevail over the difficulties mentioned above. Among these enhanced anisotropic yield criteria, the linear transformation necessitates the adoption of the chain rule in deriving the flow rule, which is also a plasticity modeling step describing the plastic flow's direction [28]. Moreover, the increase in prediction capability is relevant to the existence of the high number of parameters, and this issue can be resolved for the linear transformation-based yield criteria by increasing the order of the linear transformation, which also complicates the determination of the direction of the plastic flow [29]. On the contrary, complete polynomial-based criteria have been prominent owing to straightforward identification methodology compared to the linear transformation-based yield criteria. Therefore, the plastic flow's direction has a simple determination process, which does not dictate the chain rule.

The plasticity model has a crucial role in fracture prediction, especially for predicting the fracture initiation zone; however, the determination of the fracture initiation strain of the sheet heavily depends upon the fracture model. Fracture emergence of a ductile material involves several stages: initiation of the microcracks adjacent to the non-homogeneous locations, such as inclusions or defects, expansion of the microcracks, coalescence by the shear bands and ultimate fracture [30–32]. Researchers in the past revealed the adverse effect of the triaxial stresses on the fracture strain [33–35]. In 2003, Bao [36] conducted research involving different mechanical tests addressing different loading paths and elucidated the normalized third deviatoric stress invariant's impact on the fracture strain. Later, the third deviatoric stress invariant is correlated with the dimensionless Lode angle parameter [32]. The dimensionless stress triaxiality and the Lode parameter are the essential factors describing the related stress state, and a ductile fracture model should consist of both of them in order to predict the fracture precisely. In this regard, uncoupled phenomenological models introduced recently accounted for these parameters, and their calibration and implementation procedures are straightforward compared to the coupled models [11]. The coupled models were based upon thermodynamically consistent infrastructure, and the damage mechanism affects the hardening response of the material [37–39]. However, this feature led to the calibration procedure being more toilsome. Therefore, the utilization of the uncoupled models became more prevalent [40–42]. In recent years, enhanced ductile fracture models regarding both stress triaxiality and Lode angle parameter were introduced [43–46].

An accurate prediction of fracture initiation necessitates a convenient anisotropic plasticity model coupled with an enhanced ductile fracture model for accurate fracture initiation and FFLC prediction. In the past, certain studies considered isotropic plasticity model for ductile fracture model calibration and fracture prediction. Park et al. [41] compare the different performances of different uncoupled ductile fracture models, including Johnson-Cook, Cockcroft-Latham, Bai-Wierzbicki, MMC, and DF2012, in terms of 2D and 3D fracture loci using Mises yield criterion for a building steel EH36. Park et al. [42] also carried out a similar study for shipbuilding steels of AH36 and DH36 using the isotropic yield criterion. Kong et al. [47] performed a study on Q355 steel to the effect of different fracture models Cockcroft-Latham, Johnson-Cook, Ko-Huh, Bai-Wierzbicki, CrashFEM, and DF2012 uncoupled models. In the literature, similar studies regarding the adoption of the isotropic yield criterion can be found [40,48]. Some contemporary studies also regarded the isotropic yield criterion probably to simplify the analyses. Recently, Ding et al. [49] carried out extensive work assessing the performance of different ductile fracture models for a large variety of materials, including AA 2024-T351, AISI 1045, Q460, Mg-Al-

Zn-RE, and Ti-6Al-4 V. In this study, the authors also proposed a new fracture model. However, they used an isotropic yield criterion, and the necessity of an anisotropic yield criterion is emphasized in this research. Park et al. [50] conducted a study to characterize the fracture behavior of SUS304L steel regarding the isotropic yield criterion coupled with the Hosford-Coulomb criterion. Zheng et al. [51] adopted the isotropic yield criterion coupled with the Hosford-Coulomb ductile fracture model for characterizing the fracture mechanism of different materials involving Advanced high strength steel, stainless steel, and aluminum alloy. In these studies, the importance of the Lode parameter was indicated. There are also many studies involving anisotropic yield criteria in utilization for fracture prediction and FFLC prediction in the literature; however, they are limited, and in these studies, the fundamental anisotropic models were adopted. Kacem et al. [52] performed research on AA6061-T6 aluminum alloy regarding different temperatures by adopting the r-based Hill48 yield criterion in conjunction with the DF2012 fracture model. Zhang et al. [53] predicted the fracture loci of AA6016-T4 aluminum alloy through linear transformation-based anisotropic yield criterion (similar to a yield criterion proposed by Yld91 [54]). The research, including anisotropic yield criteria in conjunction with the ductile fracture models, also exists but concentrates on a specific forming operation, such as hole expansion [22,55,56]. Different studies can be found in the literature that take the anisotropic yield criterion coupled with a fracture model [11,19]. However, the anisotropic yield criteria used in these studies are either r-based or yield stress ratio-based and have a limited number of anisotropy parameters. These studies emphasized the significance of the anisotropic yield locus representation. However, the implementation of an advanced anisotropic yield criterion on fracture initiation prediction became a gap in the literature since the uniaxial tensile tests in high orientation numbers of more than three are required in addition to the uniaxial tensile tests with different geometrical discontinuities. The increase in the mechanical tests not only leads to an increase in the test burden and cost but also makes the calibration and optimization process of the implemented material model involving the yield criterion and fracture model combination. FFLC measures fracture initiation in a broad spectrum, and implementations that include an advanced yield criterion along with an enhanced ductile fracture model are scarce in the literature. Moreover, the utilization of the sixth-order polynomial-based anisotropic yield criterion coupled with an enhanced ductile fracture model was not encountered in the literature survey. The material's anisotropy is not only important for the FFLC prediction but also crucial for ductile fracture model calibration, since the fracture models were calibrated based on the FE simulations of the mechanical tests. Recently, the difference between the isotropic plasticity-based identification and the anisotropic plasticity-based identification of the ductile fracture model was emphasized by Li et al. [57].

This study systematically addresses the difference in ductile fracture model calibrations with respect to the isotropic and anisotropic-based yield criteria. Besides, the difference between the analytical and numerical FFLC predictions was not addressed in the literature. Although the analytical FFLC predictions are presented after calibrating the ductile fracture models [46,58], these predictions lack physical factors such as:

- The analytical predictions of FFLC in the literature are based upon the uniaxial tensile tests, in which the in-plane stresses are dominant [46,58]. The bending issue brings about a variation of stress states through thickness [17]. In the physical Nakajima test, the deformation is done by the vertical motion of the punch, leading to a biaxial tension state at the top surface of the sheet, where the fracture is expected to initiate. Correspondingly, the out-of-plane effects in the physical forming tests involving bending processes are disregarded in the analytical approach.
- The friction-lubrication conditions, which affecting the formability limits.
- The geometry of the die tools, the radius of the punch and die, draw bead or blank holder force, etc.
- Although the anisotropy of the sheet is regarded in the calibration of the ductile fracture model in the literature (In the numerical simulations of the notched specimens for comparing the experimental and numerical force–displacement outcomes in order to obtain the fracture model parameters), the sheet's anisotropy in the physical test is not regarded in the analytical predictions of FFLC, which may affect the fracture initiation location on the sheet. Considering that the anisotropy plays a vital role in stress and strain distributions on the sheet, the predicted fracture initiation zone can be changed with respect to the isotropic and anisotropic sheet assumptions.

Accordingly, the literature studies focusing on the analytical predictions of FFLC and the effect of physical conditions have been ignored, and this situation leads to another gap in the literature, which is the reliability of the analytical predictions. In the numerical simulations, the issues explained above are taken into consideration in the FFLC predictions, which are also the subjects focused on in this study. Besides, a material model including an anisotropic plasticity model (regarding the anisotropic feature's directionalities accurately) and a ductile fracture model (regarding the stress triaxiality and Lode parameter's effect) is required for introduction to a FE solver with an implicit stress update scheme coupled with return mapping algorithm. These solvers are compelling for implementing new material cards due to the high number of computations [13–15]. Besides, the material models incorporated into the software should be capable of accounting for the deformation-based anisotropy accompanied by the fracture mechanism. The implicit algorithms provide a better reflection of anisotropic properties in the numerical FE simulations; however, an advanced material model is always mandatory for anisotropic plasticity and ductile fracture representations in engineering and industrial applications. The most difficult challenge is coupling the advanced anisotropic plasticity models and advanced ductile fracture models when including them in FE solvers, especially with implicit stress update schemes. The reason is that the identification procedures of anisotropic plasticity models coupled with ductile fracture require computational, experimental, and optimization efforts simultaneously. The anisotropic plasticity model necessitates the standard uniaxial tensile tests in different material's orientations, while the uniaxial tensile tests and FE simulations of different specimens having dissimilar geometrical discontinuities are required in order to calibrate a ductile fracture model. In addition, advanced models require higher mechanical tests, which increase the optimization burden. Finally, the theoretical background and the calibrated model should be included in the FE solver through Fortran-based user-defined material subroutines.

This process involves the knowledge of mechanical testing, material science, and computer science, as well as computational efforts. Therefore, this process is a multidisciplinary procedure. This issue points out another gap in the literature, which is assembling an advanced anisotropic yield criterion and fracture model and implementing it into an implicit FE solver such as Marc employing both global and local implicit formulas to predict the field variables, which are essential to predict fracture initiation reliably.

This study was conducted to give insights into gaps determined from the literature survey and explained in detail above meticulously. The current research assesses the difference between the FLC predictions by anisotropic identification methodology criterion and isotropic calibration methodology for two specific DP steels, DP600 and DP800. The difference between the analytical and numerical FFLC predictions, the impact of the numerical factors, and the role of the sheet's anisotropy on the FFLC prediction were thoroughly investigated. The HomPol6 anisotropic yield criterion was implemented so as to represent the shape of the yield locus for the anisotropic identification methodology, while the DF2016 ductile fracture model was implemented to predict fracture initiation in analytical and numerical approaches. Both the HomPol6 yield criterion and the DF2016 fracture model were incorporated into the Marc FE solver through the Hypela2 user-defined material subroutine generated in the Fortran programming language to perform the Nakajima test analyses and acquire the numerical FFLC. Initially, the analytical results of anisotropic and isotropic identification methodologies were compared; afterward, the Nakajima test simulations were carried out, and the role of the numerical factors was evaluated.

2. Material and method

This section explains the experimental procedures, constitutive anisotropic plasticity modeling and the calibration of the implemented model.

2.1. Experimental procedure

This section explains the uniaxial tensile tests carried out so as to adjust the hardening response, ductile fracture model, and anisotropic plasticity model calibrations. The standard uniaxial tensile tests were conducted in an Instron 8872 test apparatus with a 25 kN loading capacity. The 0.7 mm thick DP600 and 1.17 mm thick DP800 steels were utilized in tensile testing. The specimens were procured through the laser cutting method for seven directions with 15° intervals (From the rolling direction to the transverse direction), and all the specimens were pulled up to the fracture at a constant rate of 1.10^{-4} s^{-1}. For each direction, three specimens were procured and tested for reproducibility. The dimensions of the standard tensile test specimens were given in a previous study by Akşen et al. [59]. Fig. 1 and Fig. 2 show the test apparatus, the uniaxial tensile test specimen's geometry, the fractured test specimens, and the repeated test results in rolling direction respectively.

Yield stress ratio and r value (Lankford's coefficients) directionalities are the crucial anisotropy features in plasticity. r values represent the resistance against thinning and tearing in related material's orientation. For r value determination, the specimens were pulled up to a constant elongation limit of 0.1 strain. Then, the r values were obtained in line with the ASTM E517-19 specifications [60]. The following equation is employed to determine the r values.

$$r_\theta = \frac{\ln \frac{w}{w_0}}{\ln \frac{t}{t_0}} \tag{1}$$

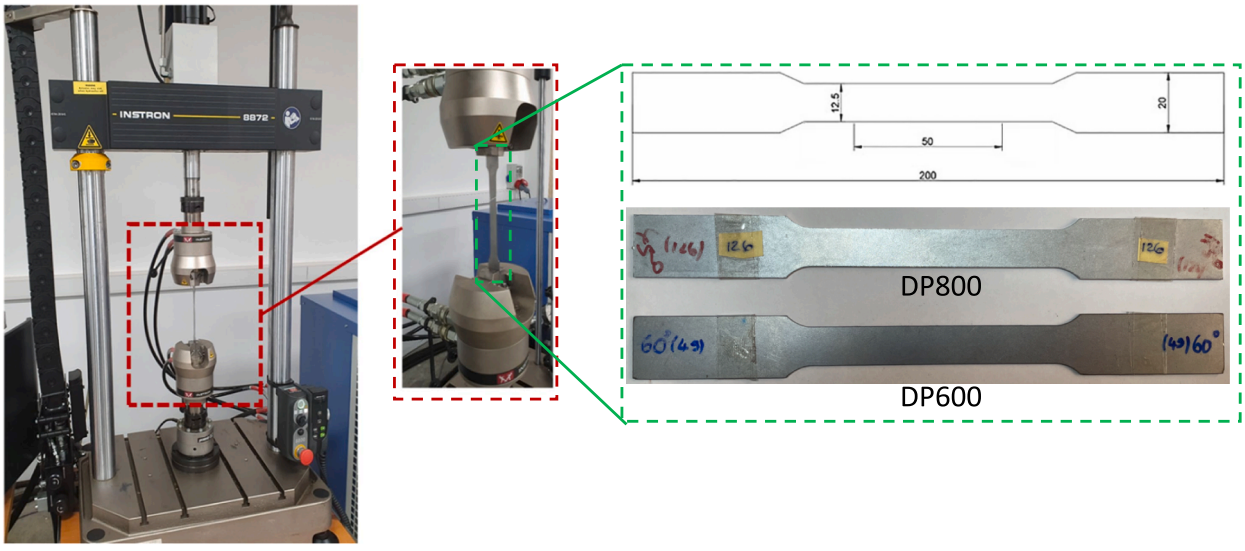

Fig. 1. Instron tensile testing machine and the standard uniaxial test specimen's geometry.

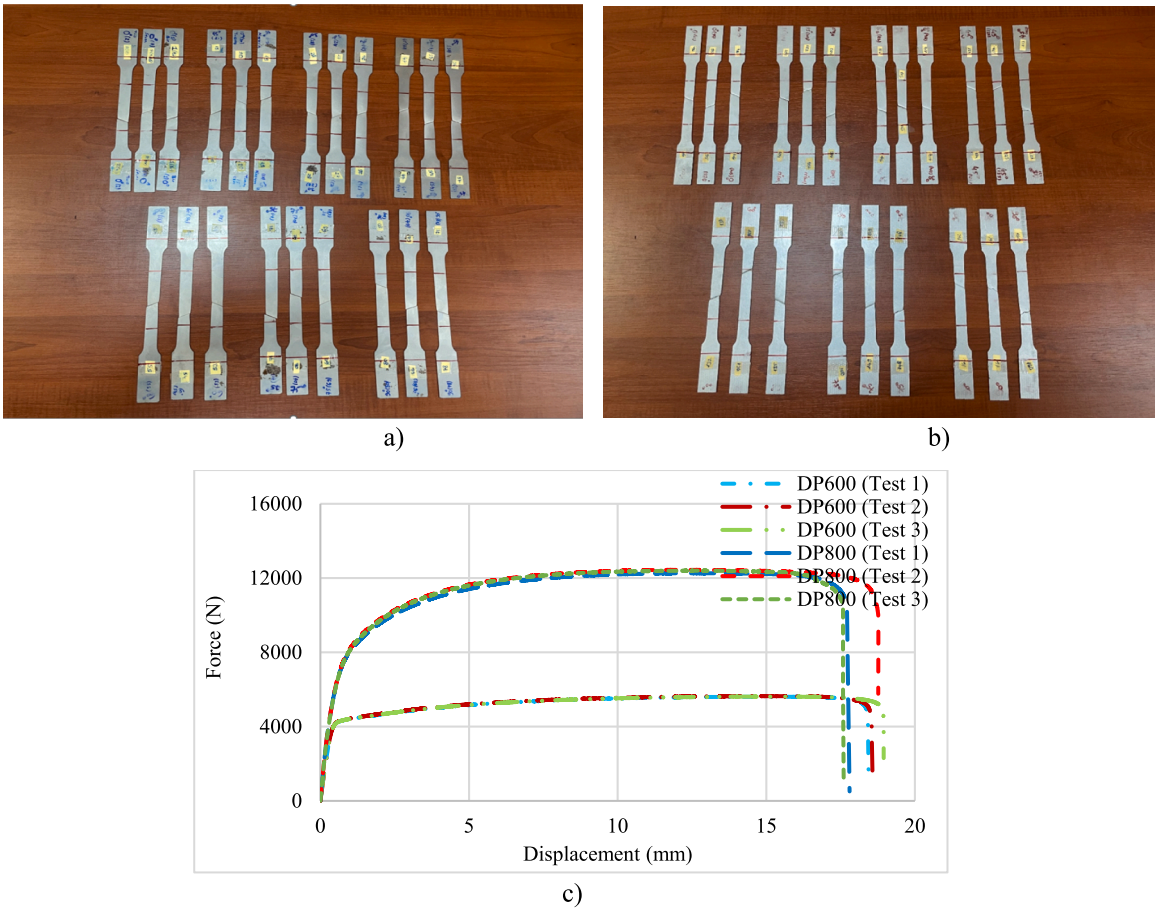

Fig. 2. Fractured standard tensile test specimens: a) DP600, b) DP800, c) force–displacement curves of both steels standard uniaxial tensile tests in rolling direction.

here, w represents the width of the specimen, while t denotes the thickness (w_0 and t_0 are the initial width and thickness of the tensile test specimens). Besides, θ represents the related material's orientation covering from the rolling direction ($\theta = 0°$) to transverse direction ($\theta = 90°$). As for the yield stress determinations in different orientations, the stress value corresponding to the 0.002 strain value (%0.2) was specified as the yield stress in each orientation. Afterward, the hardening features of both DP steels were attained via curve fitting methodology in Matlab software. The curve fitting procedure performed based on the Swift approach (Eq. (2)) and Fig. 3 illustrates the fitted curves. In this procedure, the rolling direction was taken into consideration.

$$\sigma_0 = C(\varepsilon_0 + \varepsilon_p)^p \tag{2}$$

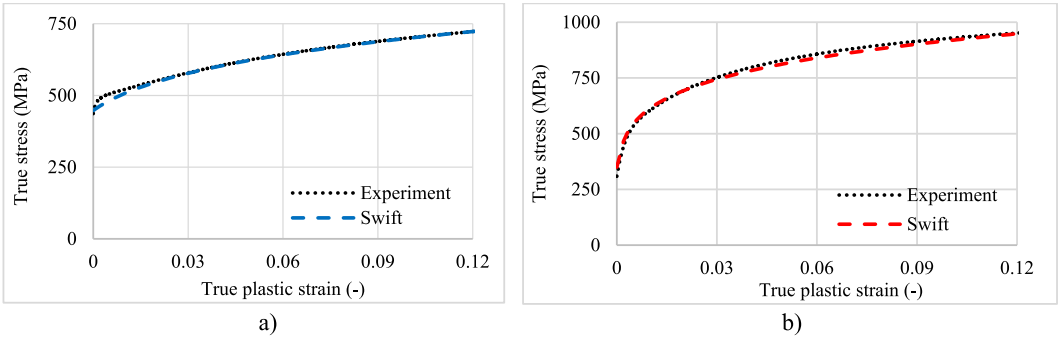

Fig. 3. Swift hardening curves of DP steels: a) DP600, b) DP800.

in Eq. (2), C, ε_0 and p are the hardening curve parameters associated with the Swift Law. In curve fitting procedure, the range between the yield strength and the ultimate tensile strength were regarded. The parameters C and p are 1071 MPa and 0.194, respectively for DP600 steel, while 1375 MPa and 0.175 for DP800 steel. Afterwards, the standard uniaxial tests were repeated up to an identical displacement value for determining the anisotropic features. These tests were also conducted three times in each direction for reproducibility. The r values (Lankford coefficients) and yield strengths were acquired on these specimens. The acquired data were listed in Table 1 and Table 2.

Here, the subscripts 0, 15, 30, 45, 60, 75, and 90 denote the orientation of the sheet (θ). The yield stresses (σ) and Lanford coefficients (r) were acquired along these orientations, covering from the rolling direction (θ = 0°) to the transverse direction (θ = 90°) with the 15° intervals. Besides, the yield stress values in different orientations (σ_θ) were normalized through dividing these values by reference yield stress in the rolling direction (σ_0). The chemical decompositions of the DP steels were also given in Table 3.

The volume fractions of ferrite and martensite constituents were acquired by scanning electron microscope. For DP600 steel, the ferrite ratio was 70.8 %, while the martensite was 28.7 %. The bainite constituent was measured 0.5 %. The average grain sizes of ferrite and martensite were measured 4.8 and 1.3 μm, respectively. As for the DP800 steel, ferrite and martensite volume fractions are 64.1 % and 35.3 %, respectively. The bainite had a 0.6 % ratio, which can be neglectable compared to the ferrite and martensite. The average grain sizes of ferrite and martensite for DP800 steel were measured 4.2 and 1.6 μm. The increase in martensite in DP steels results in an increase in strength, as seen in Fig. 3, while a decrease in ductility, as seen in Fig. 2c. In Fig. 2c, test 3 of DP800 steel exhibited higher ductility compared to tests 1 and 2; however, on average, the ductility of DP800 steel was blatantly less than DP600 steel.

In the final stage, the uniaxial tensile tests of notched specimens representing different loading conditions were carried out in order to calibrate the fracture model. In this framework, four different sample geometries were cut along rolling direction (0° orientation) by an electro-discharging machine on both steels. These samples are shear (SH), hole-centered (CH), and radius-shaped notched (NT) specimens (10 mm and 20 mm radius). These specimens and their dimensions are given in Fig. 4.

These specimens were chosen in order to characterize the different loading conditions. The shear sample and the centered hole specimens represent the pure shear and uniaxial tension zones, respectively, while the radius-shaped notched specimens represent the high triaxiality region. In analogy to the standard test specimens, three samples for each notch shape were cut, and the tensile tests of these notched samples were repeated three times to ensure the reliability of the force–displacement responses.

2.2. Plasticity modeling

A plasticity model is essential for addressing the deformation behavior beyond the yield strength. The boundary of plastic deformation onset in different stress states, the variation of this bound, and the relation between the stress and strain increment during the plastic flow are compulsorily defined in forming operations where the plastic deformation is prominent. An anisotropic plasticity model is necessitated to tackle the mechanical feature's variation in different orientations.

The Mises isotropic yield criterion is adopted first in this work for comparison purposes to highlight the influence of the anisotropic yield locus presentation from the isotropic one. The Mises criterion is given below.

$$f_{Mises} = \sqrt{\sigma'_{ij} : \sigma'_{ij}} - \sqrt{\frac{2}{3}}\sigma_0 = 0 \tag{3}$$

here, σ'_{ij} denotes the deviatoric stress components, and σ_0 is the flow stress. In the current research, an anisotropic plasticity model is incorporated into the constitutive model through an anisotropic yield criterion, and in this study, the sixth-order complete homogeneous polynomial-based yield criterion (HomPol6) is implemented. This criterion includes 16 adjustable parameters, most of which are adjusted via an optimization method ensuring convexity and positivity. This criterion addresses the major numerical issues, such as producing convex yield locus boundary, anomalous behavior, etc., encountered in sheet metal forming operations [23,25,61,62]. Furthermore, this criterion's high number of coefficients will be essential for high anisotropic feature predictions (r value and yield stress ratios) in the current research. The straightforward form of the polynomial-based criteria has a relatively simple derivation process for determining the plastic flow's direction [28]. The yield criterion of the HomPol6 is given in Eq. (4).

$$\begin{aligned} f_{HomPol6} = [&a_1\sigma_{xx}^{\,6} + a_2\sigma_{xx}^{\,5}\sigma_{yy} + a_3\sigma_{xx}^{\,4}\sigma_{yy}^{\,2} + a_4\sigma_{xx}^{\,3}\sigma_{yy}^{\,3} + a_5\sigma_{xx}^{\,2}\sigma_{yy}^{\,4} + a_6\sigma_{xx}\sigma_{yy}^{\,5} + a_7\sigma_{yy}^{\,6} \\ &+ \left(a_8\sigma_{xx}^{\,4} + a_9\sigma_{xx}^{\,3}\sigma_{yy} + a_{10}\sigma_{xx}^{\,2}\sigma_{yy}^{\,2} + a_{11}\sigma_{xx}\sigma_{yy}^{\,3} + a_{12}\sigma_{yy}^{\,4}\right)\sigma_{xy}^{\,2} + \left(a_{13}\sigma_{xx}^{\,2} + a_{14}\sigma_{xx}\sigma_{yy} + a_{15}\sigma_{y}^{\,2}\right)\sigma_{xy}^{\,4} + a_{16}\sigma_{xy}^{\,6}]^{\frac{1}{6}} - \sigma_0 \end{aligned} \tag{4}$$

in the equation above, the parameters denoted a_1 and a_7 are specified based on the yield conditions in sheet's rolling and transverse directions, while the a_2 a_6 are computed with respect to the experimental r-values along the same directions [28,61]. The remaining

Table 1
Yield strength ratios of the DP steels.

Material	σ_0/σ_0	σ_{15}/σ_0	σ_{30}/σ_0	σ_{45}/σ_0	σ_{60}/σ_0	σ_{75}/σ_0	σ_{90}/σ_0	σ_b/σ_0
DP600	1	1.005	0.957	0.946	0.951	0.932	0.940	1
DP800	1	1.001	1.023	1.022	1.027	1.011	1.025	1

Table 2
Lankford's coefficients (r values) of the DP steels.

Material	r_0	r_{15}	r_{30}	r_{45}	r_{60}	r_{75}	r_{90}	r_b
DP600	0.86	0.85	0.74	0.96	0.76	0.60	1.02	1
DP800	0.75	0.89	0.98	0.74	0.70	0.85	0.84	1

Table 3
Chemical decompositions (%wt) of the DP steels.

Material	C	Mn	Cr	Si	P	Ni
DP600	0.094	1.620	0.034	0.060	<0.01	0.02
DP800	0.105	1.550	0.024	0.200	0.017	0.01

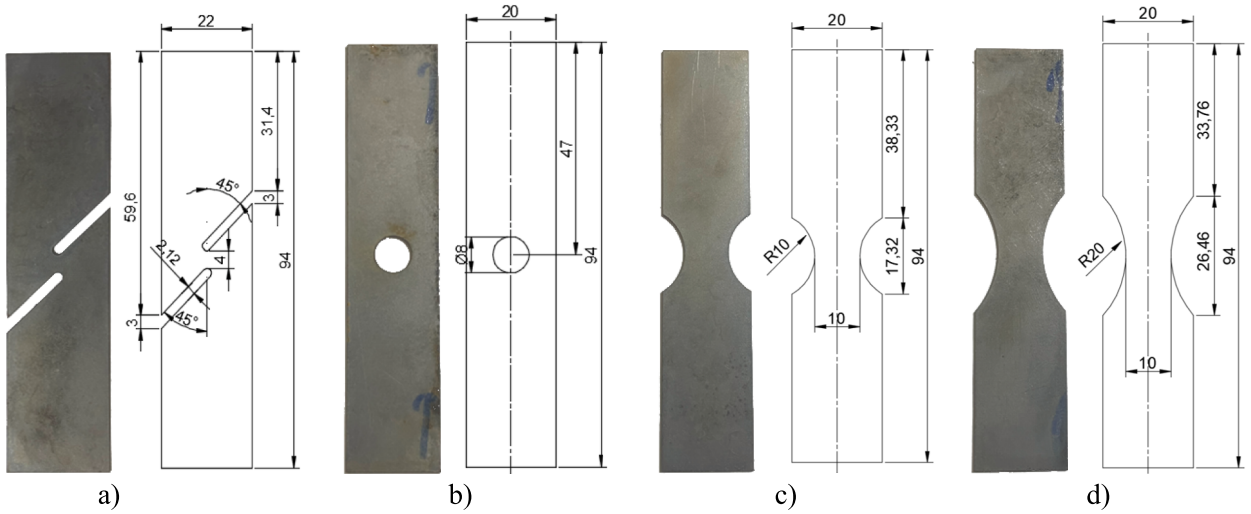

Fig. 4. Notched tensile test samples a) SH, b) CH, c) NT10, d) NT20.

parameters were identified through the minimization of the objective function given below.

$$\mathrm{Obj} = \sum w_1\left(\frac{(\sigma_\theta)_1^{pr}}{(\sigma_\theta)_1^{exp}} - 1\right)^2 + \sum w_2\left(\frac{(r_\theta)_2^{pr}}{(r_\theta)_2^{exp}} - 1\right)^2 + w_3\left(\frac{(\sigma_b)_3^{pr}}{(\sigma_b)_3^{exp}} - 1\right)^2 + w_4\left(\frac{(r_b)_4^{pr}}{(r_b)_4^{exp}} - 1\right)^2 \tag{5}$$

The least-square optimization method was adopted to minimize the objective function. Separate weight functions controlled each component in this equation. For DP800 steel, the weight functions were selected to be equal, while for DP600 steel, the weights were distributed for each orientation, and the specific orientations of 30° and 60° directions were increased compared to 15° and 75° directions in order to ensure the best fit since the scatters of experimental data were more blatant than DP800. To this end, the weight value w1 and w2 were disintegrated into seven components. Since the yield criterion is two times differentiable, during the identification process, the Hessian matrix is controlled to be higher than zero for ensuring the convexity of the yield locus [28]. The coefficients $w_{1\text{-}4}$ are the weights allocated for different anisotropic features, including the r value directionality, yield stress directionality and biaxial data. For an arbitrary orientation, the yield stress ratio can be expressed as in Eq. (6).

$$\sigma_\theta^{pr} = \frac{\sigma_0}{Cf_\theta\left(\sigma_{xx} = \sigma_\theta \cos^2\theta,\ \sigma_{yy} = \sigma_\theta \sin^2\theta,\ \sigma_{xy} = \sigma_\theta \cos\theta \sin\theta\right)} \tag{6}$$

Note that cos = c and sin = s, the coefficient function of HomPol6 (Cfθ) is as follows.

$$Cf\theta_{HomPol6} = \left(a_1c^{12} + a_2c^{10}s^2 + a_3c^8s^4 + a_4c^6s^6 + a_5c^4s^8 + a_6c^2s^{10} + a_7s^{12} + \left(a_8c^8 + a_9c^6s^2 + a_{10}c^4s^4 + a_{11}c^2s^6 + a_{12}s^8\right)c^2s^2 + \left(a_{13}c^4 + a_{14}c^2s^2\theta + a_{15}s^4\right)c^4s^4 + a_{16}c^6s^6\right)^{\frac{1}{6}} \tag{7}$$

In analogy to the yield stress prediction, the r value expression along an arbitrary direction is given in Eq. (8).

$$r_\theta^{pr} = \frac{d\varepsilon_{xx}^p \sin^2\theta + d\varepsilon_{yy}^p \cos^2\theta - d\varepsilon_{xy}^p \cos\theta \sin\theta}{-\left(d\varepsilon_{xx}^p + d\varepsilon_{yy}^p\right)} \tag{8}$$

The biaxial yield stress and r-value can be estimated as follows.

$$\sigma_b^{pr} = \frac{\sigma_0}{\mathrm{Cf}_b\left(\sigma_{xx}=\sigma_b,\ \sigma_{yy}=\sigma_b,\ \ \sigma_{xy}=0\right)} \tag{9}$$

$$r_b^{pr} = \frac{\frac{\partial f_{HomPol6}}{\partial \sigma_{xx}}\left(\sigma_{xx}=\sigma_b,\ \sigma_{yy}=\sigma_b,\ \sigma_{xy}=0\right)}{\frac{\partial f_{HomPol6}}{\partial \sigma_{yy}}\left(\sigma_{xx}=\sigma_b,\ \sigma_{yy}=\sigma_b,\ \sigma_{xy}=0\right)} \tag{10}$$

where the coefficient function of HomPol6 for balanced biaxial loading is,

$$\mathrm{Cf}_b\left(\sigma_{xx}=\sigma_b,\sigma_{yy}=\sigma_b,\sigma_{xy}=0\right) = \left(a_1+a_2+a_3+a_4+a_5+a_6+a_7\right)^{\frac{1}{6}} \tag{11}$$

In addition to the calibration procedure explained above, the convexity condition of HomPol6 yield function was introduced into the optimization procedure. In this regard, all the minors of Hessian matrix should be positive. The Hessian matrix of HomPol6 is given below.

$$\mathbb{H} = \begin{bmatrix} \frac{\partial^2 f_{HomPol6}}{\partial \sigma_x^2} & \frac{\partial^2 f_{HomPol6}}{\partial \sigma_x \partial \sigma_y} & \frac{\partial^2 f_{HomPol6}}{\partial \sigma_x \partial \sigma_{xy}} \\ \frac{\partial^2 f_{HomPol6}}{\partial \sigma_y \partial \sigma_x} & \frac{\partial^2 f_{HomPol6}}{\partial \sigma_{yy}^2} & \frac{\partial^2 f_{HomPol6}}{\partial \sigma_y \partial \sigma_{xy}} \\ \frac{\partial^2 f_{HomPol6}}{\partial \sigma_{xy} \partial \sigma_x} & \frac{\partial^2 f_{HomPol6}}{\partial \sigma_{xy} \partial \sigma_y} & \frac{\partial^2 f_{HomPol6}}{\partial \sigma_{xy}^2} \end{bmatrix} \tag{12}$$

The principal minors should be positive, which yields.

$$\mathbb{H}_1 = \frac{\partial^2 f_{HomPol6}}{\partial \sigma_{xx}^2} > 0 \tag{13}$$

$$\mathbb{H}_2 = \begin{vmatrix} \frac{\partial^2 f_{HomPol6}}{\partial \sigma_{xx}^2} & \frac{\partial^2 f_{HomPol6}}{\partial \sigma_{xx} \partial \sigma_{yy}} \\ \frac{\partial^2 f}{\partial \sigma_{yy} \partial \sigma_{xx}} & \frac{\partial^2 f}{\partial \sigma_{yy}^2} \end{vmatrix} > 0 \tag{14}$$

$$\mathbb{H}_3 = \begin{vmatrix} \frac{\partial^2 f_{HomPol6}}{\partial \sigma_{xx}^2} & \frac{\partial^2 f_{HomPol6}}{\partial \sigma_{xx} \partial \sigma_{yy}} & \frac{\partial^2 f_{HomPol6}}{\partial \sigma_{xx} \partial \sigma_{xy}} \\ \frac{\partial^2 f_{HomPol6}}{\partial \sigma_{yy} \partial \sigma_{xx}} & \frac{\partial^2 f_{HomPol6}}{\partial \sigma_{yy}^2} & \frac{\partial^2 f_{HomPol6}}{\partial \sigma_{yy} \partial \sigma_{xy}} \\ \frac{\partial^2 f_{HomPol6}}{\partial \sigma_{xy} \partial \sigma_{xx}} & \frac{\partial^2 f_{HomPol6}}{\partial \sigma_{xy} \partial \sigma_{yy}} & \frac{\partial^2 f_{HomPol6}}{\partial \sigma_{xy}^2} \end{vmatrix} > 0 \tag{15}$$

The positivity-convexity condition was introduced as constraint for calibrating the HomPol6 parameters in the optimization step. The plastic strain's increment is dictated by the associated flow rule Eq. (16).

$$\mathrm{d}\varepsilon_{ij}^{p} = \mathrm{d}\lambda \frac{\mathrm{df}_{\mathrm{HomPol6}}}{\mathrm{d}\sigma_{ij}} \tag{16}$$

in Eq. (16), $\mathrm{d}\lambda$ is the plastic multiplier. Under the associated flow rule, the plastic flow's directions for both HomPol6 and Mises yield criteria are different. Further, the equivalent plastic strain equations are dissimilar. Regarding the principal stress state, the principal strain components of HomPol6 can be obtained as follows considering the associated flow rule.

$$\begin{aligned} \mathrm{d}\varepsilon_{xx}^{p} = \frac{1}{6}[&a_1\sigma_{xx}{}^6 + a_2\sigma_{xx}{}^5\sigma_{yy} + a_3\sigma_{xx}{}^4\sigma_{yy}{}^2 + a_4\sigma_{xx}{}^3\sigma_{yy}{}^3 + a_5\sigma_{xx}{}^2\sigma_{yy}{}^4 + a_6\sigma_{xx}\sigma_{yy}{}^5 + a_7\sigma_{yy}{}^6 + \left(a_8\sigma_{xx}{}^4 + a_9\sigma_{xx}{}^3\sigma_{yy} + a_{10}\sigma_{xx}{}^2\sigma_{yy}{}^2\right. \\ &\left.+a_{11}\sigma_{xx}\sigma_{yy}{}^3 + a_{12}\sigma_{yy}{}^4\right)\sigma_{xy}{}^2 + \left(a_{13}\sigma_{xx}{}^2 + a_{14}\sigma_{xx}\sigma_{yy} + a_{15}\sigma_y{}^2\right)\sigma_{xy}{}^4 + a_{16}\sigma_{xy}{}^6]^{-\frac{5}{6}}[6a_1\sigma_{xx}^5 + 5a_2\sigma_{xx}^4\sigma_{yy} + 4a_3\sigma_{xx}^3\sigma_{yy}^2 \\ &+ 3a_4\sigma_{xx}^2\sigma_{yy}^3 + 2a_5\sigma_{xx}\sigma_{yy}^4 + a_6\sigma_{yy}^5 + \sigma_{xy}^2\left(4a_6\sigma_{xx}^3 + 3a_9\sigma_{xx}^2\sigma_{yy} + 2a_{10}\sigma_{xx}\sigma_{yy}^2 + a_{11}\sigma_{yy}^3\right) + \sigma_{xy}^4\left(2a_{13}\sigma_{xx} + a_{14}\sigma_{yy}\right)] \end{aligned} \tag{17}$$

$$d\varepsilon_{yy}^{p} = \frac{1}{6}[a_1{\sigma_{xx}}^6 + a_2{\sigma_{xx}}^5\sigma_{yy} + a_3{\sigma_{xx}}^4{\sigma_{yy}}^2 + a_4{\sigma_{xx}}^3{\sigma_{yy}}^3 + a_5{\sigma_{xx}}^2{\sigma_{yy}}^4 + a_6\sigma_{xx}{\sigma_{yy}}^5 + a_7{\sigma_{yy}}^6 + \left(a_8{\sigma_{xx}}^4 + a_9{\sigma_{xx}}^3\sigma_{yy}\right.$$
$$\left.+a_{10}{\sigma_{xx}}^2{\sigma_{yy}}^2 + a_{11}\sigma_{xx}{\sigma_{yy}}^3 + a_{12}{\sigma_{yy}}^4\right){\sigma_{xy}}^2 + \left(a_{13}{\sigma_{xx}}^2 + a_{14}\sigma_{xx}\sigma_{yy} + a_{15}{\sigma_{y}}^2\right){\sigma_{xy}}^4 + a_{16}{\sigma_{xy}}^6]^{-\frac{5}{6}}[a_2\sigma_{xx}^5 + 2a_3\sigma_{xx}^4\sigma_{yy}$$
$$+ 3a_4\sigma_{xx}^3\sigma_{yy}^2 + 4a_5\sigma_{xx}^2\sigma_{yy}^3 + 5a_6\sigma_{xx}\sigma_{yy}^4 + 6a_7\sigma_{yy}^5 + \sigma_{xy}^2\left(a_9\sigma_{xx}^3 + 2a_{10}\sigma_{xx}^2\sigma_{yy} + 3a_{11}\sigma_{xx}\sigma_{yy}^2 + 4a_{12}\sigma_{yy}^3\right) + \sigma_{xy}^4\left(a_{14}\sigma_{xx} + 2a_{14}\sigma_{yy}\right)] \tag{18}$$

$$d\varepsilon_{xy}^{p} = \frac{1}{6}[a_1{\sigma_{xx}}^6 + a_2{\sigma_{xx}}^5\sigma_{yy} + a_3{\sigma_{xx}}^4{\sigma_{yy}}^2 + a_4{\sigma_{xx}}^3{\sigma_{yy}}^3 + a_5{\sigma_{xx}}^2{\sigma_{yy}}^4 + a_6\sigma_{xx}{\sigma_{yy}}^5 + a_7{\sigma_{yy}}^6 + \left(a_8{\sigma_{xx}}^4 + a_9{\sigma_{xx}}^3\sigma_{yy}\right.$$
$$\left.+a_{10}{\sigma_{xx}}^2{\sigma_{yy}}^2 + a_{11}\sigma_{xx}{\sigma_{yy}}^3 + a_{12}{\sigma_{yy}}^4\right){\sigma_{xy}}^2 + \left(a_{13}{\sigma_{xx}}^2 + a_{14}\sigma_{xx}\sigma_{yy} + a_{15}{\sigma_{y}}^2\right){\sigma_{xy}}^4 + a_{16}{\sigma_{xy}}^6]^{-\frac{5}{6}}[2\sigma_{xy}\left(a_8{\sigma_{xx}}^4 + a_9{\sigma_{xx}}^3\sigma_{yy}\right. \tag{19}$$
$$\left.+ a_{10}{\sigma_{xx}}^2{\sigma_{yy}}^2 + a_{11}\sigma_{xx}{\sigma_{yy}}^3 + a_{12}{\sigma_{yy}}^4\right) + 4\sigma_{xy}^3\left(a_{13}{\sigma_{xx}}^2 + a_{14}\sigma_{xx}\sigma_{yy} + a_{15}{\sigma_{yy}}^2\right) + 6a_{16}{\sigma_{xy}}^5]$$

Regarding the in-plane components, the principal strain increments can be calculated by following expressions

$$d\varepsilon_1^p = \frac{d\varepsilon_{xx}^p + d\varepsilon_{yy}^p}{2} + \sqrt{\left(\frac{d\varepsilon_{xx}^p - d\varepsilon_{yy}^p}{2}\right)^2 + \left(d\varepsilon_{xy}^p\right)^2} \tag{20}$$

$$d\varepsilon_2^p = \frac{d\varepsilon_{xx}^p + d\varepsilon_{yy}^p}{2} - \sqrt{\left(\frac{d\varepsilon_{xx}^p - d\varepsilon_{yy}^p}{2}\right)^2 + \left(d\varepsilon_{xy}^p\right)^2} \tag{21}$$

Regarding the plastic incompressibility the third principal plastic strain component can be determined as follows.

$$d\varepsilon_3^p = -\left(d\varepsilon_1^p + d\varepsilon_2^p\right) \tag{22}$$

The equivalent plastic strain increment can be determined using Eq. (16).

$$d\varepsilon_{eqv}^p = \sqrt{\frac{2}{3}\left(d\varepsilon_1^p d\varepsilon_1^p + d\varepsilon_2^p d\varepsilon_2^p + d\varepsilon_3^p d\varepsilon_3^p\right)} \tag{23}$$

Based on the co-rotational plasticity the strain decomposition is governed by the following expression. In this study, additive decomposition, corresponding to the disintegration of the strain increment into elastic and plastic components is assumed.

$$d\varepsilon_{ij} = d\varepsilon_{ij}^{els} + d\varepsilon_{ij}^{pls} \tag{24}$$

Since the mechanical tensile tests were conducted in 10^{-4} s^{-1}, the quasi-static conditions were assumed. Based on the calibration methodology explained above, the adjusted HomPol6 parameters were listed in Table 4. In addition, the parameter set, which the HomPol6 criterion reduces to Mises isotropic criterion is also provided in Table 4.

The performance of a yield criterion is tested in terms of the anisotropic feature predictions. Therefore, the analytical predictions of HomPol6 compared with experimental outcomes for both steels are demonstrated in Figs. 5-7 for r value directionality, yield stress ratio directionality, and yield locus, respectively.

A yield criterion is expected to demonstrate accurate analytical estimations. In this regard, the yield locus constructed by the yield criterion should be convex for the uniqueness of the plastic flow's direction for dissimilar loading paths. The HomPol6 criterion produces a convex yield locus for both materials. Since this study explores the difference between the isotropic and anisotropic identification processes of the ductile fracture models, the yield loci were compared with the Mises yield loci. Although the isotropic

Table 4
HomPol6 parameters.

	DP600 HomPol6	DP800 HomPol6	Isotropic Case
a_1	1	1	1
a_2	−2.77	−2.57	−3
a_3	6.03	4.79	6
a_4	−7.95	−5.30	−7
a_5	7.64	4.58	6
a_6	−4.40	−2.36	−3
a_7	1.45	0.86	1
a_8	10.71	7.67	9
a_9	−8.90	−18.28	−18
a_{10}	−0.55	35.06	27
a_{11}	−7.53	−16.22	−18
a_{12}	10.26	9.21	9
a_{13}	24.61	27.67	27
a_{14}	6.32	−38.29	−27
a_{15}	26.60	19.64	27
a_{16}	27	27	27

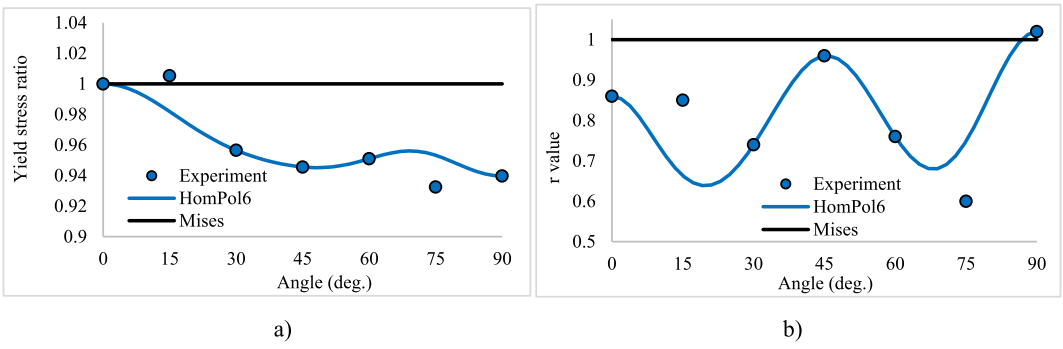

a) b)

Fig. 5. Analytical HomPol6 a) yield stress ratio and b) r value directionalities of DP600 steel.

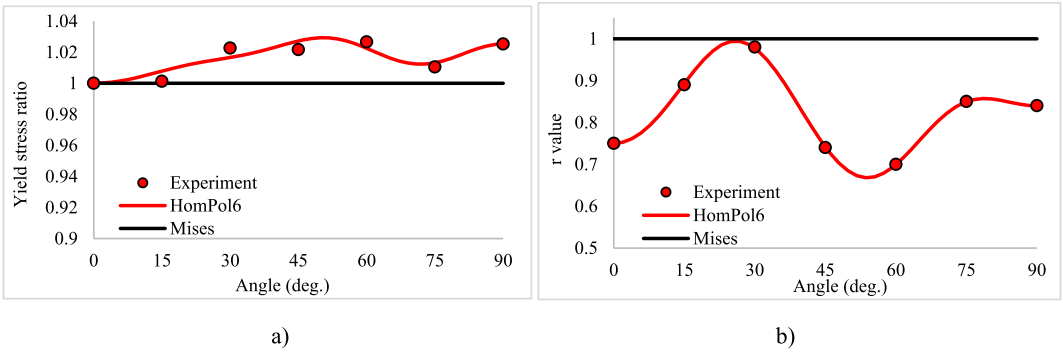

a) b)

Fig. 6. Analytical HomPol6 a) yield stress ratio and b) r value directionalities of DP800 steel.

and anisotropic yield loci seem close to each other, significant deviations were blatantly observed for both steels, especially for DP600 in distinct stress states that are focused in Fig. 7a for DP600 and Fig. 7b for DP800 steel. The difference between the yield loci mainly stems from the dissimilarities of yield stress with respect to different stress states. Only the yield stress in the transverse direction can be noticed from the yield locus, where the deviations were observed in both materials for both isotropic and anisotropic yield criteria assumptions (Fig. 7a and b). Furthermore, the HomPol6 exhibited successful predictions for DP800, especially for r-value directionalities. Even though the performance of DP600 is quite accurate, discrepancies were encountered along 15° and 75°. This situation results from the abrupt variations of the experimental data for DP600 due to the considerable anisotropy. For DP600, the experimental r values vary between 0.6 and 1 (Fig. 5b), while for DP800 steel, the experimental r values change from 0.7 to 1 (Fig. 6b), which indicates noticeable anisotropic effects for both steels. Besides, the experimental yield stress ratios were also varied in both steels, especially for DP600 (decreasing toward 0,93 approximately in Fig. 5a). In Figs. 5 and 6, the difference between the isotropic Mises and anisotropic HomPol6 are evident since the isotropic Mises criterion predicts constant value of 1 in all r value and yield stress directionalities. Considering that the anisotropy is a measure of the variation of the mechanical features with respect to the material's different orientations, both materials demonstrated a significant anisotropic effect. In general, the HomPol6 criterion showed good agreements for both steels.

2.3. *Ductile fracture modeling*

A plasticity model cannot predict fracture initiation, and a ductile fracture model is a prerequisite for predicting the incipient fracture. The recently proposed phenomenological fracture model involves two crucial effects linked to the hydrostatic stress and Lode angle θ. A geometric representation of the pi-plane (π plane) and the Lode angle θ is illustrated in Fig. 8 [32,47].

These two effects are included in the fracture models through the stress triaxiality (η) and Lode parameter (L). These essential parameters are acquired based on the following equations.

$$\eta = \frac{\sigma_m}{\sigma_{eq}} \tag{25}$$

$$L = \sqrt{3}\tan\theta \tag{26}$$

σ_m denotes the mean stress and the angle θ represents the angle between the reference pure shear line and the projection of the loading path onto the pi-plane. The pi-plane involves the stress components inducing shape distortion called deviatoric stresses (σ_{ij}).

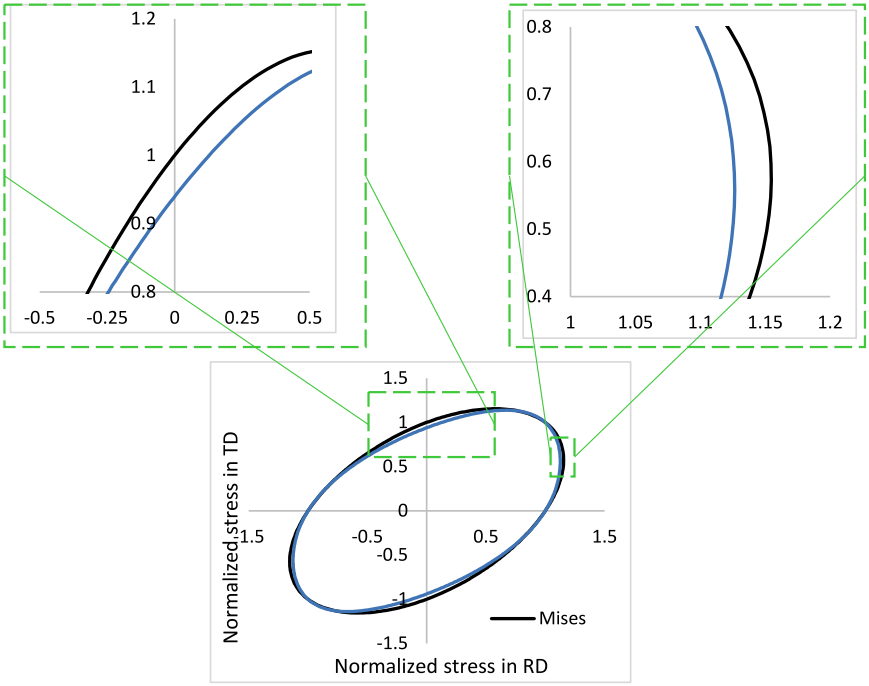

a)

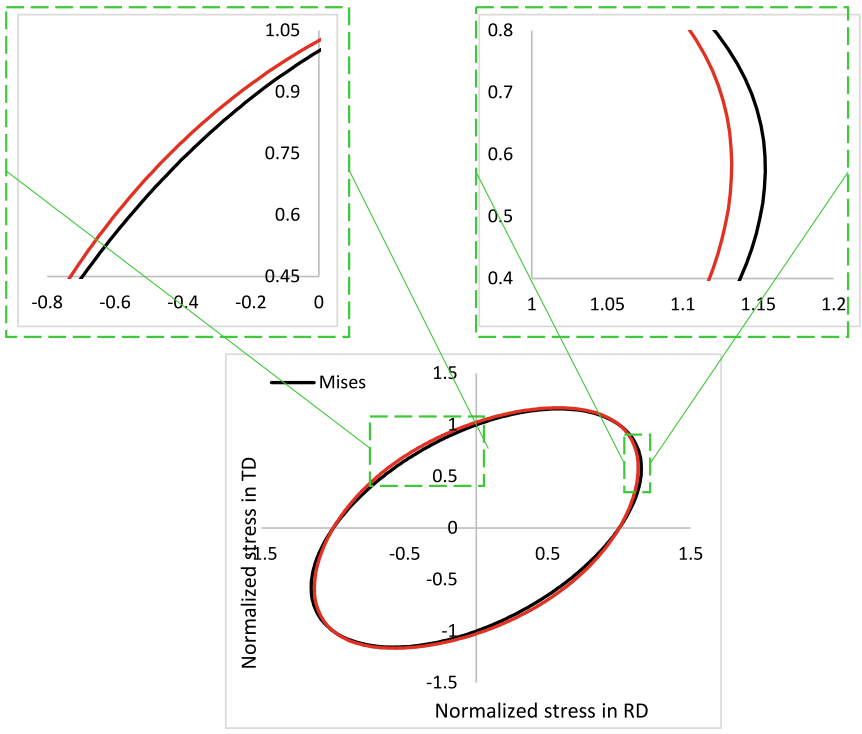

b)

Fig. 7. Analytical HomPol6 yield loci, a) DP600, b) DP800.

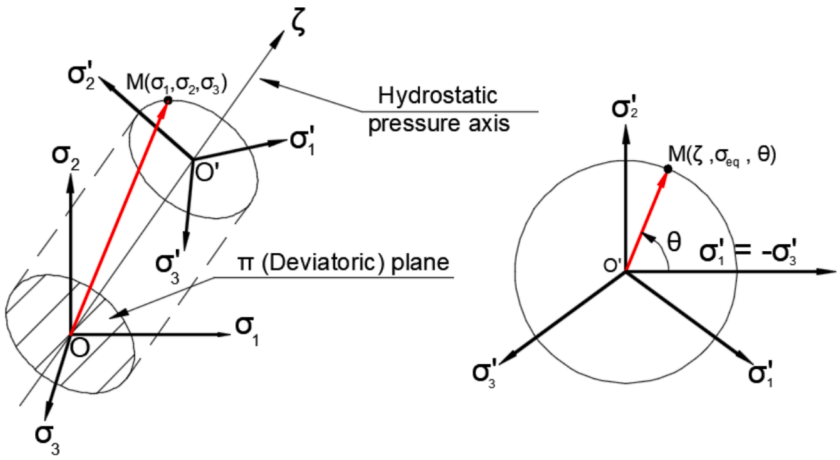

Fig. 8. Geometric representation of pi-plane and Lode angle θ.

$$\sigma_m = \frac{\sigma_1 + \sigma_2 + \sigma_3}{3} \tag{27}$$

$$\sigma'_{ij} = \sigma_{ij} - \sigma_m I \tag{28}$$

Ductile fracture comprises several stages: void generation, expansion, and coalescence [30]. Lou and co-workers [44,63] proposed a fracture model including the influences of the aforementioned stages. Later, Lou et al. [46,64,65] improved the initial model and developed new criteria. Among them, DF2016 was implemented in this research due to the enhanced prediction performance with a high number of parameters. These parameters provide the prediction performance along the pure shear and low triaxiality zone [51]. The equivalent plastic strain to fracture of the DF2016 criterion is expressed in Eq. (29).

$$\varepsilon^p_{eqf}(\eta, L)_{DF2016} = \frac{b_3}{\left(\frac{2}{\sqrt{L^2+3}}\right)^{b_1}\left(< \frac{v(\eta,L,b)}{v\left(\frac{1}{3},-1,b\right)} >\right)^{b_2}} \tag{29}$$

In the equation above, function v is given below.

$$v(\eta, L, b) = \eta + b_4 \frac{3 - L}{3\sqrt{L^2+3}} + b \tag{30}$$

The parameters $b_{1\text{-}4}$ are adjustable, and the b is associated with the cut-off value [46]. The reason opting for the DF2016 criterion was that this model is capable of predicting the intermediate and low triaxiality regions in the literature studies and the superiority of this model is tested by comparing this model with different advanced fracture models [58,65]. Besides, in this research, three different ductile fracture models were also implemented to reinforce the prediction performance of DF2016. These models are the Void Growth Model (VGM) [35], Maximum Shear Stress (MSS) [32], and Modified Coulomb-Mohr (MMC) [32,40]. The equivalent plastic fracture strains were given in Eqs. (31)–(33) according to these criteria. Among these models, VGM involves only the triaxiality effect, MSS includes only the Lode parameter's effect, and MMC predicts both features simultaneously.

$$\varepsilon^p_{eqf}(\eta)_{VGM} = c_1 e^{(-c_2\eta)} \tag{31}$$

$$\varepsilon^p_{eqf}(L)_{MSS} = \left(\frac{C}{A\sqrt{L^2+3}}\right)^{-\frac{1}{p}} \tag{32}$$

$$\varepsilon^p_{eqf}(\eta, L)_{MMC} = \left[\frac{C}{d_2}\left[d_3 + \frac{\sqrt{3}}{2-\sqrt{3}}(1-d_3)\left(\sqrt{\frac{3+L^2}{3}} - 1\right)\right]\left[\sqrt{\frac{1+d_1^2}{3+L^2}} + d_1\left(\eta + \frac{1}{3}\frac{-L}{\sqrt{3+L^2}}\right)\right]\right]^{-\frac{1}{p}} \tag{33}$$

here, the material parameters c_1, and c_2 are related to the VGM, A is related to the MSS and d_1, d_2 and d_3 are associated with the MMC ductile fracture models. The parameters C and p seen in the MSS, and MMC models represent the Swift hardening law parameters explained in Eq. (2). These parameters should also be adjusted as in the $b_{1\text{-}4}$ in DF2016 model and determined based on the FE analyses of notched tensile specimens representing dissimilar loading paths.

2.4. Partially anisotropic fracture modeling

The anisotropic fracture models can be categorized into two groups: partially [66,67] and fully anisotropic fracture models [68]. In partially anisotropic models, the yield criterion in the plasticity model is anisotropic, while the fracture model is isotropic [66]. On the other hand, in the fully anisotropic model, both the plasticity model and fracture model are anisotropic. In both methodologies, the equivalent stress for the anisotropic yield criterion is employed and embedded in the stress triaxiality and fracture model definitions [69]. For fully anisotropic models, in addition to the required tests of partially anisotropic models, the notched tensile test samples should be cut in different directions and tested. Despite these models having the potential to enhance the prediction performance, the additional tests and calibration procedures increase the cost and time consumption, which restricts usage, especially in industrial applications. Therefore, the partially anisotropic models were extensively utilized in the industry and provided good approximations even for aluminum alloys [70]. In this section, the relation between the DF2016 fracture model and anisotropic yield criterion was established. The equivalent stress of HomPol6 in 2D form is,

$$\sigma_{eq-HomPol6}^{(2D)} = \left[a_1{\sigma_{xx}}^6 + a_2{\sigma_{xx}}^5\sigma_{yy} + a_3{\sigma_{xx}}^4{\sigma_{yy}}^2 + a_4{\sigma_{xx}}^3{\sigma_{yy}}^3 + a_5{\sigma_{xx}}^2{\sigma_{yy}}^4 + a_6\sigma_{xx}{\sigma_{yy}}^5 + a_7{\sigma_{yy}}^6 + \left(a_8{\sigma_{xx}}^4 + a_9{\sigma_{xx}}^3\sigma_{yy} + a_{10}{\sigma_{xx}}^2{\sigma_{yy}}^2 + a_{11}\sigma_{xx}{\sigma_{yy}}^3 + a_{12}{\sigma_{yy}}^4\right){\sigma_{xy}}^2 + \left(a_{13}{\sigma_{xx}}^2 + a_{14}\sigma_{xx}\sigma_{yy} + a_{15}{\sigma_y}^2\right){\sigma_{xy}}^4 + a_{16}{\sigma_{xy}}^6\right]^{\frac{1}{6}} \tag{34}$$

The equation above is extended in this research to 3D form regarding the following condition [28,61,71].

$$\sigma_{eq-HomPol6}^{(3D)}(\sigma_{xx},\sigma_{yy},\sigma_{zz},\sigma_{xy},\sigma_{yz},\sigma_{zx}) = \sqrt{\left[\sigma_{eq-HomPol6}^{(2D)}(\sigma_{xx}-\sigma_{zz},\sigma_{yy}-\sigma_{zz},\sigma_{xz})\right]^2 + 2k_5\sigma_{yz}^2 + 2k_6\sigma_{zx}^2} \tag{35}$$

This expansion produces a convex yield function when the 2D yield criterion is convex. The parameters k_5 and k_6 are positive parameters related to the out-of-plane shear anisotropy. Since obtaining a tensile test specimen in the thickness direction is impossible, these parameters are picked out to assume isotropy through thickness similar to the Hill48 criterion [71]. The anisotropic stress triaxiality can be written as follows.

$$A = \frac{\sigma_{eq-HomPol6}^{(3D)}}{|\sigma_1 - \sigma_3|} \tag{36}$$

In order to simplify the derivation, parameter A can be defined as follows.

$$\eta_A = \frac{\sigma_m}{A|\sigma_1 - \sigma_3|} \tag{37}$$

The anisotropic stress triaxiality can also be expressed by the following chain rule [12].

$$\eta_A = \frac{\sigma_m}{\sigma_{eq-HomPol6}^{(3D)}} = \frac{\sigma_m}{\sigma_{eq-Mises}}\frac{\sigma_{eq-Mises}}{\sigma_{eq-HomPol6}^{(3D)}} \tag{38}$$

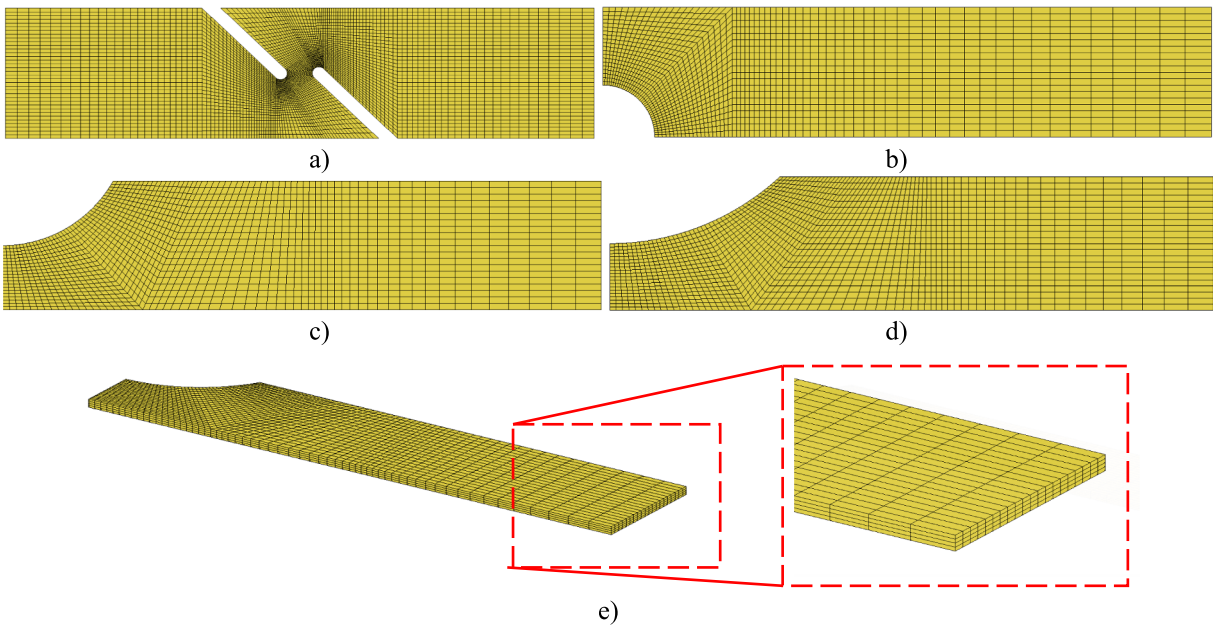

Fig. 9. FE models of notched tensile specimens, a) SH, b) CH, c) NT10, d) NT20, e) elements through thickness.

In sheet metal forming, the stress state acting on the blank sheet can be assumed as plane stress where $\sigma_3 = 0$. In addition, if the Eq. (25) is included in Eq. (38) the anisotropic triaxiality can be written as follows.

$$\eta_A = \eta \frac{\sqrt{L^2 + 3}}{2A} \tag{39}$$

Correspondingly the Cauchy stress components can be written in the form of,

$$\sigma_1 = (\eta_A + \frac{3 - L}{A})\sigma^{(3D)}_{eq-HomPol6} \tag{40}$$

$$\sigma_2 = (\eta_A + \frac{2L}{A})\sigma^{(3D)}_{eq-HomPol6} \tag{41}$$

$$\sigma_3 = (\eta_A - \frac{3 + L}{A})\sigma^{(3D)}_{eq-HomPol6} \tag{42}$$

Finally, the Eq. (39) and Eqs. (40)–(42) are included in the Eq. (29) and Eq. (30), the expanded form of Eq. (29) can be expressed as in Eq. (43).

$$\varepsilon^p_{eqf}(\eta_A, L)_{DF2016} = \frac{b_3}{(\frac{1}{A})^{b_1}(< \frac{\eta_A + b_4\frac{3-L}{A} + b}{\frac{2}{3} + b_4\frac{1}{3A} + b} >)^{b_2}} \tag{43}$$

2.5. FE analyses of notched tensile specimens and parameter calibration of DF2016

Since each test leads to a different stress state, the equivalent plastic fracture strain should be acquired from the corresponding test. However, the FE force–displacement responses should be consistent with the experimental behavior so as to ensure the reliability of the adjusted parameters linked to the fracture model. The specimens having different geometrical discontinuities were explained in Section 2.1, Experimental Procedure. In this framework, the FE models of the specimens demonstrated in Fig. 3 were generated (Fig. 9) with through thickness mesh discretization and pulled up to the fracture point. In the mesh discretization of the notched samples fully integrated constant dilatational free from shear-volume locking hexahedral solid elements (Hex7 in Marc FE software) were used. The elements were intensified toward the critical zones where a crack or fracture initiation is expected. Besides, uniaxial tensile tests were carried out on isotropic and anisotropic yield criteria. The comparative force–displacement results were illustrated in Figs. 10-13 for both steels.

According to Figs. 10-13, the isotropic and anisotropic force–displacement results were close to each other. Besides, both results were compatible with the experimental outcomes, especially for DP600. The correlation of the SH sample of DP800 was in good agreement with the experiment; however, slight deviations were observed for the other samples of DP800. Overall, the force–displacement comparisons showed the reliability of the hardening behavior and subsequent data acquisition along with the identification procedure of the fracture model. The equivalent plastic fracture strain values were procured from the FE simulations of each notched sample. The maximum values equivalent to plastic fracture strains for NT10 and NT20 were observed at the center of the narrowed sections of the samples, near the hole at the center of the thickness for CH, and at the surface of the SH specimen. These observations are also consistent with the literature studies [41,47]. The occurrence of maximum stress triaxiality level at the center of these samples (for CH, NT10, and NT20) leads to the fracture initiation inside of the specimens since the stress triaxiality causes the growth of the holes [46]. Therefore, it is impossible to capture the initial major crack leading to the fracture, even with sophisticated measuring devices [41,46]. Besides, even if the fracture initiates at the surface (In SH specimen, maximum equivalent plastic fracture strain is observed at the surface in this study), it was reported in the literature that it is difficult to capture the exact fracture initiation

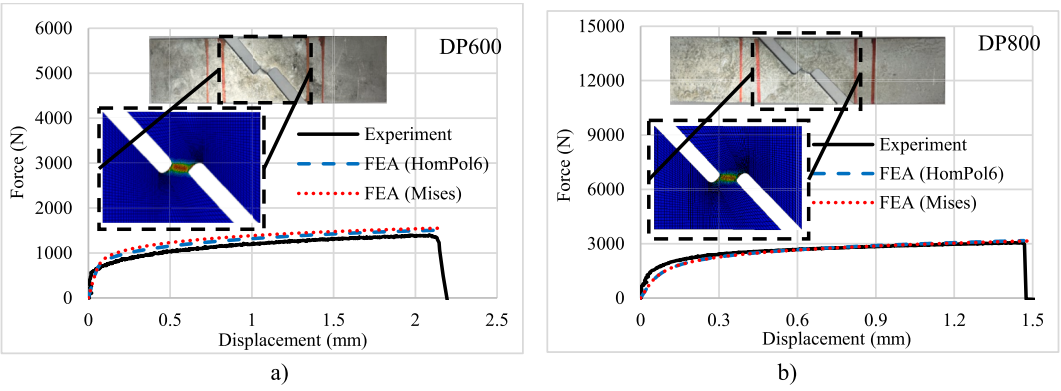

Fig. 10. Comparative results of SH samples, a) DP600, b) DP800.

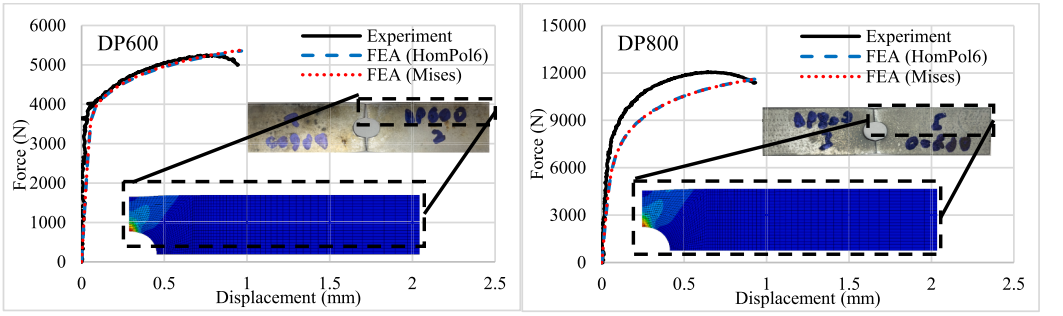

Fig. 11. Comparative results of CH samples, a) DP600, b) DP800.

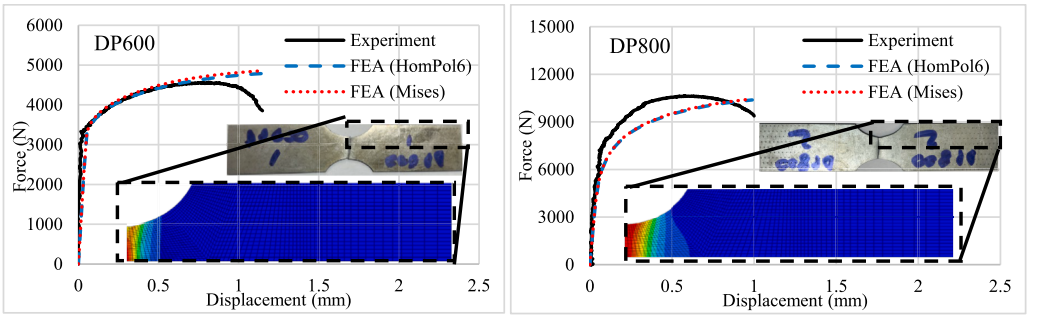

Fig. 12. Comparative results of NT10 samples, a) DP600, b) DP800.

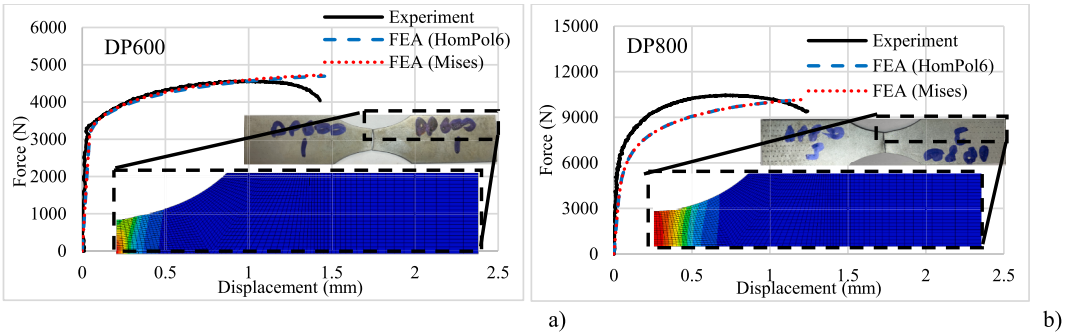

Fig. 13. Comparative results of NT20 samples, a) DP600, b) DP800.

location [41]. Since the crack propagates rapidly and fracture takes place abruptly, measuring the strain between the local band formation and the fracture is difficult, even with sophisticated methodologies, such as digital image correlation systems or optical measurement systems. Therefore, the displacement values corresponding to the sudden decrease in the force–displacement curves for each specimen are regarded to be the initiation of the fracture [41,46].

In the identification procedure, the stress triaxiality and Lode parameters that vary during the tensile testing analyses should be determined to correlate the determined fracture strain with the corresponding stress state. The stress triaxiality and Lode parameter evolutions are presented in Figs. 14 and 15, respectively.

As seen in Figs. 14 and 15, the difference in isotropic and anisotropic analysis results is more blatant for DP600 steel when compared to the DP800. For DP800 steel, the results were close except for the SH sample. Since the DP600 steel is more ductile and anisotropic relative to DP800 (considering the yield locus and yield stress directionality), the effect of triaxial stresses might be more obvious. Fig. 14a and Fig. 15a (DP600 results) also point out that although the force–displacement behaviors of isotropic and anisotropic approaches are similar, the difference in stress triaxiality and Lode parameters may be significant. Hence, the variation of the stress triaxiality and Lode parameters were acquired from the FE simulations and the average values were determined using Eqs. (44) and (45). For each specimen, the maximum equivalent plastic fracture strain value corresponding to the fracture point along the

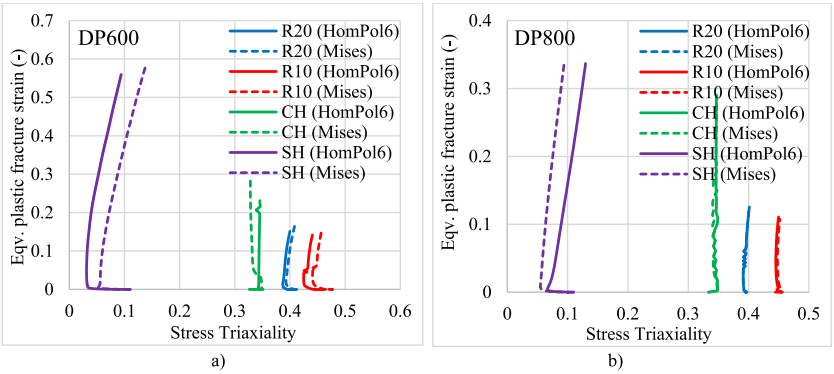

Fig. 14. Variation of the stress triaxiality during the deformation of the notched samples, a) DP600, b) DP800.

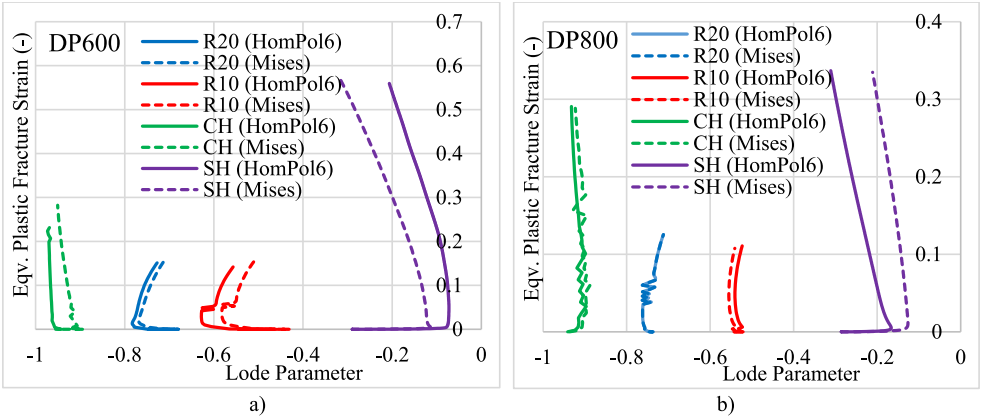

Fig. 15. Variation of the Lode parameter during the deformation of the notched samples, a) DP600, b) DP800.

Table 5
The parameters acquired from the tensile testing simulations of DP600 steel sheet.

DP600	SH		CH		NT10		NT20	
	HomPol6	Mises	HomPol6	Mises	HomPol6	Mises	HomPol6	Mises
$\varepsilon_{eq.f}^{pls}$	0.560	0.578	0.231	0.282	0.142	0.154	0.151	0.164
η_{ave}	0.054	0.089	0.344	0.333	0.423	0.449	0.392	0.399
L_{ave}	−0.124	−0.202	−0.966	−0.933	−0.595	−0.549	−0.761	−0.744

Table 6
The parameters acquired from the tensile testing simulations of DP800 steel sheet.

DP800	SH		CH		NT10		NT20	
	HomPol6	Mises	HomPol6	Mises	HomPol6	Mises	HomPol6	Mises
$\varepsilon_{eq.f}^{pls}$	0.337	0.335	0.291	0.288	0.111	0.103	0.126	0.125
η_{ave}	0.029	0.022	0.346	0.344	0.447	0.449	0.395	0.395
L_{ave}	−0.246	−0.163	−0.918	−0.908	−0.535	−0.551	−0.742	0.742

geometrical discontinuity was acquired from the FE simulations separately with respect to isotropic and anisotropic calibration methodologies. The determined parameters prerequisite for the fracture loci construction were summarized in Tables 5 and 6 for both steel sheets separately.

$$\eta_{ave} = \frac{1}{\varepsilon_{eq.f}^{pls}} \int_0^{\bar{\varepsilon}_f} \eta(\varepsilon_{eq}^{pls}) d\varepsilon_{eq}^{pls} \tag{44}$$

$$L_{ave} = \frac{1}{\varepsilon^{pls}_{eq,f}} \int_0^{\bar{\varepsilon}_f} L(\varepsilon^{pls}_{eq}) d\varepsilon^{pls}_{eq} \quad (45)$$

As seen in the findings of DP600, the equivalent plastic fracture strain, the average stress triaxiality, and Lode parameters are noticeably dissimilar for the outcomes of the isotropic and anisotropic yield criteria. Regarding the force–displacement responses are quite close, the differences in these parameters are striking. The constructed fracture loci for both yield criteria approach elucidated the effect of the identification method's influence in Fig. 16 for both steels. The calibrated parameters are also presented in Table 7.

The fracture loci results showed that the identification procedure has an impact on the fracture initiation, and the impact may be more evident for anisotropic materials. In general, the strain values for each specimen are close in magnitude; however, the anisotropy changed the triaxiality and Lode parameters noticeably. The variation of the equivalent plastic fracture strain values in isotropic and anisotropic yield criteria for identical notched specimens is illustrated in Fig. 15. These changes affected the fracture initiation limit, especially for DP600 steel. For less anisotropic materials, the variation became minor. 3D fracture loci were generated and presented in Figs. 17 and 18 for a deeper evaluation.

Despite the fact that the shapes of the 3D fracture loci were similar, the difference in magnitudes is expectedly noticeable for DP600 steel. For DP800, the differences can be seen in normalized tension and compression lines where the Lode parameter is −1 and 1, respectively. However, the effect of anisotropic calibration is striking for DP600 steel. For $\eta = 0$ (zero triaxiality), the equivalent plastic fracture strain is 2 for anisotropic calibration, while 3.1 for isotropic calibration along the normalized uniaxial compression line. These values are approximately 0.8 for anisotropic calibration, 1 for isotropic calibration for the $L = 0$ line. A difference is also observed along the normalized uniaxial tension line. Although the difference in DP800 is lower than that of DP600, the differences along normalized tension and compression lines are noticeable.

Further, the projection of the plastic strain components on the deviatoric π-plane was acquired at different stress triaxiality levels from 0 (Pure shear) to 0.66 (Balanced biaxial tension). Figs. 19 and 20 presented these envelopes.

Since the DF2016 criterion has the Lode parameter's influence, the six-point star profiles were acquired. In addition, the DF2016 criterion includes the stress triaxiality effect, which shows its impact in width change at different triaxiality levels. The width change in different triaxiality levels were more poignant for both DP steels. Besides, the effect of anisotropy demonstrated its influence for both steels blatantly in uniaxial tension ($\theta = 330°$), balanced biaxial tension ($\theta = 30°$) lines. Similar projections can be seen in different loading conditions as well.

The performance of the DF2016 was also assessed by comparing the 2D fracture loci with different ductile fracture models. The comparative results are demonstrated in Fig. 21. Besides, the calibrated parameters for VGM, MSS, and MMC ductile fracture models were presented for DP600 and DP800 steels in Table 8.

As seen in Fig. 21, the equivalent plastic fracture strain data procured from the shear sample (SH) could only be captured by the DF2016 model for both steel sheets. Here the MSS model has one parameter to calibrate (except for the hardening parameters) and it cannot predict the fracture locus accurately. VGM includes only the triaxiality effect and only provides a reliable performance between the uniaxial tension ($\eta = 1/3$) and plane strain tension lines ($\eta = 1/\sqrt{3}$). For the rest of the fracture loci, the prediction was not consistent. The MMC involves both the triaxiality and Lode parameters effect; however, it cannot predict the shear sample's data. Different studies have also reported the lack of the MMC criterion in intermediate and negative triaxiality regions [58,65]. This comparison shows the performance of the DF2016 ductile fracture model.

3. FE modeling of Nakajima test

This study evaluates the difference between the analytical and numerical FFLC predictions. Therefore, the FE models of the

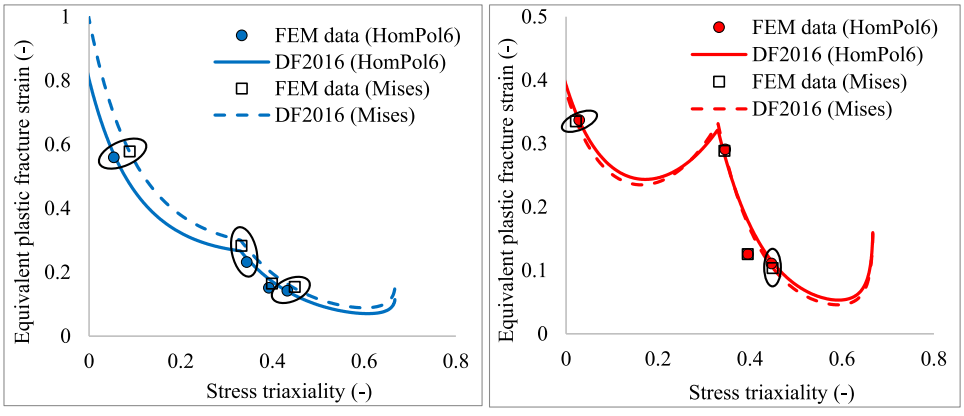

Fig. 16. Fracture loci constructed by HomPol6 and Mises yield criteria for, a) DP600, b) DP800 (The differences were shown in ellipses).

Table 7
Parameters of DF2016 fracture criteria for HomPol6 and Mises yield criteria.

DP600 (HomPol6)	DP600 (Mises)	DP800 (HomPol6)	DP800 (Mises)
$b_1 = 3.9$	$b_1 = 3.5$	$b_1 = 8.2$	$b_1 = 9.2$
$b_2 = 2.9$	$b_2 = 3.4$	$b_2 = 2.4$	$b_2 = 2.55$
$b_3 = 0.265$	$b_3 = 0.3$	$b_3 = 0.32$	$b_3 = 0.33$
$b_4 = 0.2$	$b_4 = 0.4$	$b_4 = 0.2$	$b_4 = 0.2$
$b = 0.33$	$b = 0.33$	$b = 0.33$	$b = 0.33$

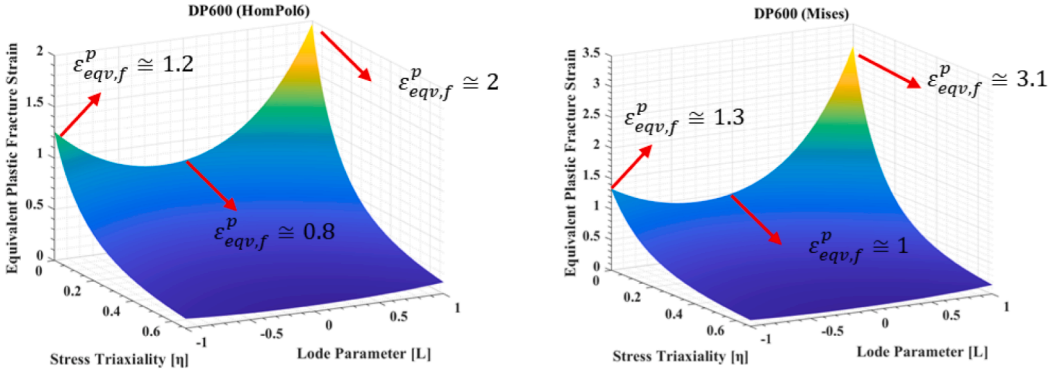

Fig. 17. 3D fracture loci constructed by a) HomPol6 and b) Mises yield criteria for DP600.

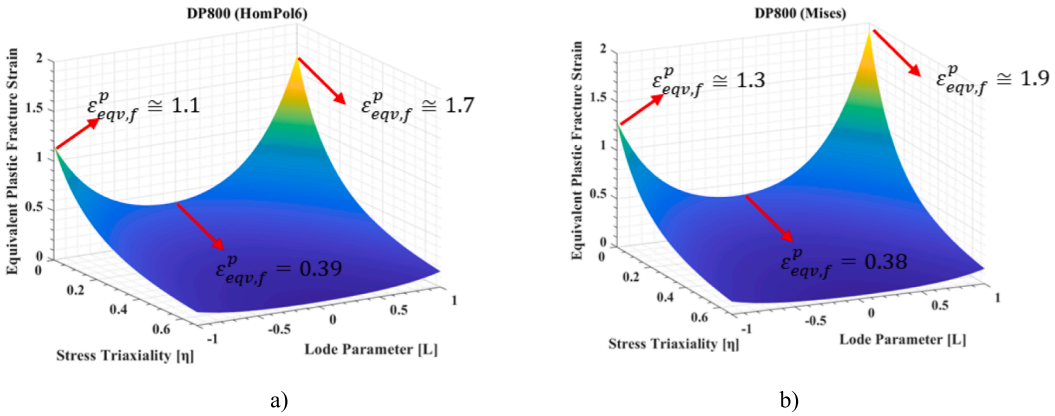

Fig. 18. 3D fracture loci constructed by a) HomPol6 and b) Mises yield criteria for DP800.

Nakajima test for different specimens with different web widths were generated and analyzed. The web width of the specimens employed in this research ranged from 20 mm to 190 mm. The dimensions of the specimens were picked out in line with a literature study [72]. Fig. 20 shows the schematic view of the specimens. The specimens with web widths of 20 mm, 40 mm, 90 mm, 100 mm, 130 mm, 160 mm, and 190 mm were considered within this scope. The specimens with web widths of 20 mm, 90 mm, and 190 mm were also illustrated along with the mesh structure through thickness in Fig. 22.

The element numbers were increased toward the critical regions where the fracture initiation was expected. The quarter section was regarded for each sample so as to avoid high CPU requirements. The samples were meshed with fully integrated constant dilatational hexahedral solid elements also known as Hex7 with four elements through thickness (For both steels) in Marc. The so-called Hex7 elements are credible for constant dilatational free from shear locking features [73,74]. Fig. 23 shows the FE model of the Nakajima test.

A draw bead is geometrically generated to restrict the sheet's flow. The friction coefficient was assumed to be 0.1 for all contact interactions. The tools were generated in Marc software as rigid geometries. In analogy to the mesh layouts, the die tools were also modeled as quarter sections. For each sample, the simulations were conducted for both DP steels. Fracture initiation was considered when the damage accumulation reached 100 %, which corresponded that the equivalent plastic fracture strain reached the reciprocal

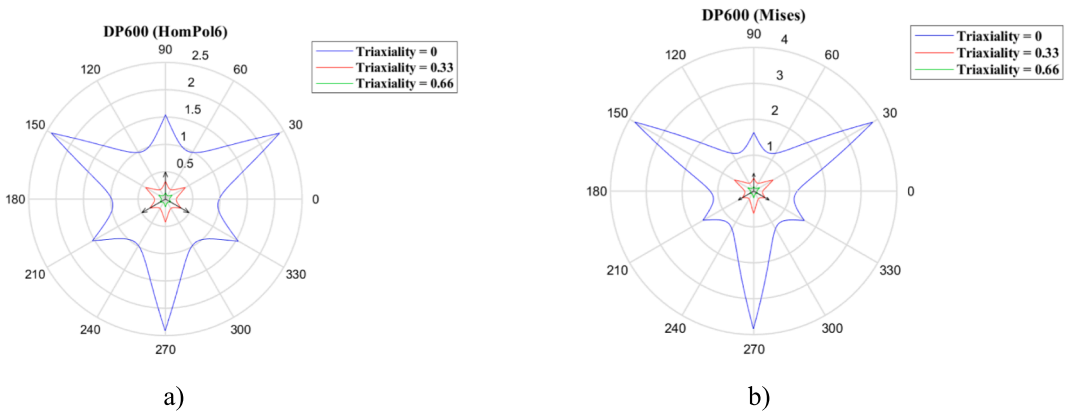

Fig. 19. Strain envelopes constructed by a) HomPol6 and b) Mises yield criteria for DP600.

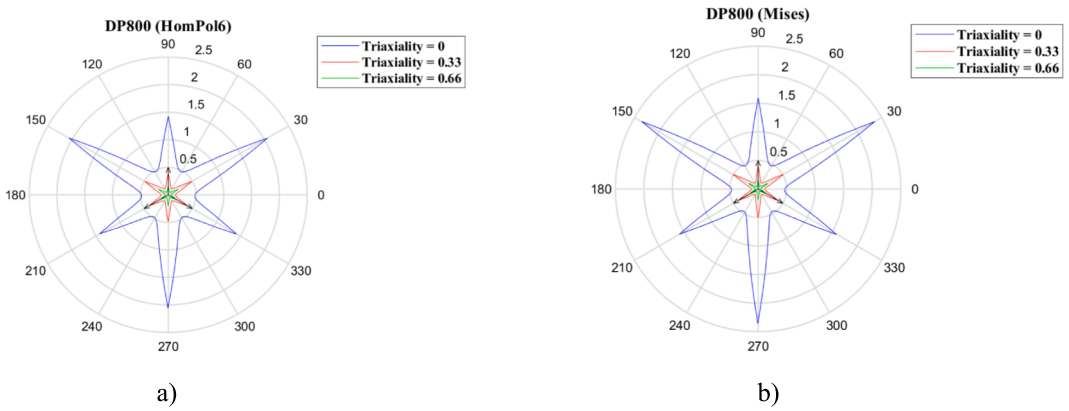

Fig. 20. 3D fracture loci constructed by a) HomPol6 and b) Mises yield criteria for DP800.

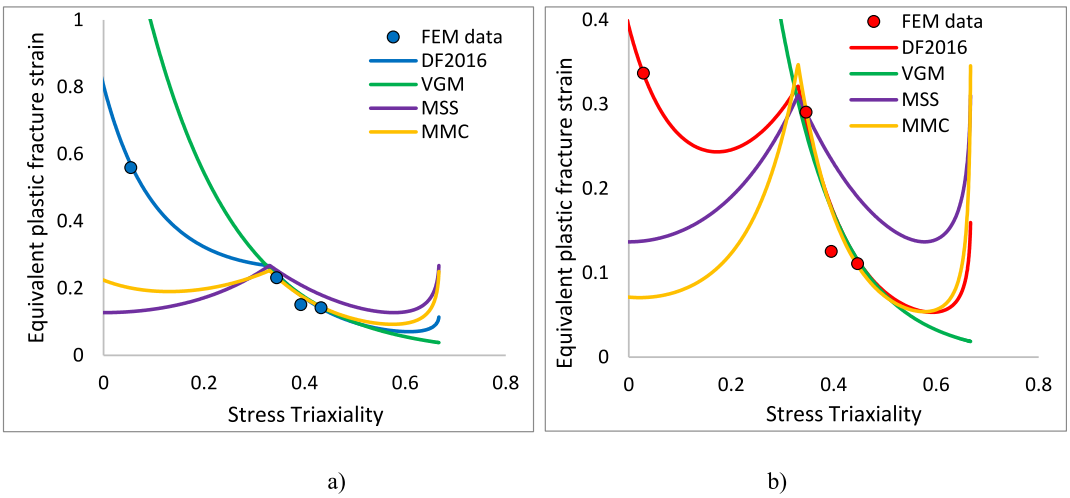

Fig. 21. Comparison of different fracture models for, a) DP600, b) DP800 steels.

Table 8
Parameters of fracture models for DP steels.

Material	Fracture Model	Parameters		
	MSS	A = 415 MPa		
DP600	VGM	$c_1 = 1.70$	$c_2 = 5.7$	
	MMC	$d_1 = 0.19$	$d_2 = 495$	$d_3 = 1.05$
	MSS	A = 560 MPa		
DP800	VGM	$c_1 = 4.70$	$c_2 = 8.30$	
	MMC	$d_1 = 0.05$	$d_2 = 600$	$d_3 = 1.20$

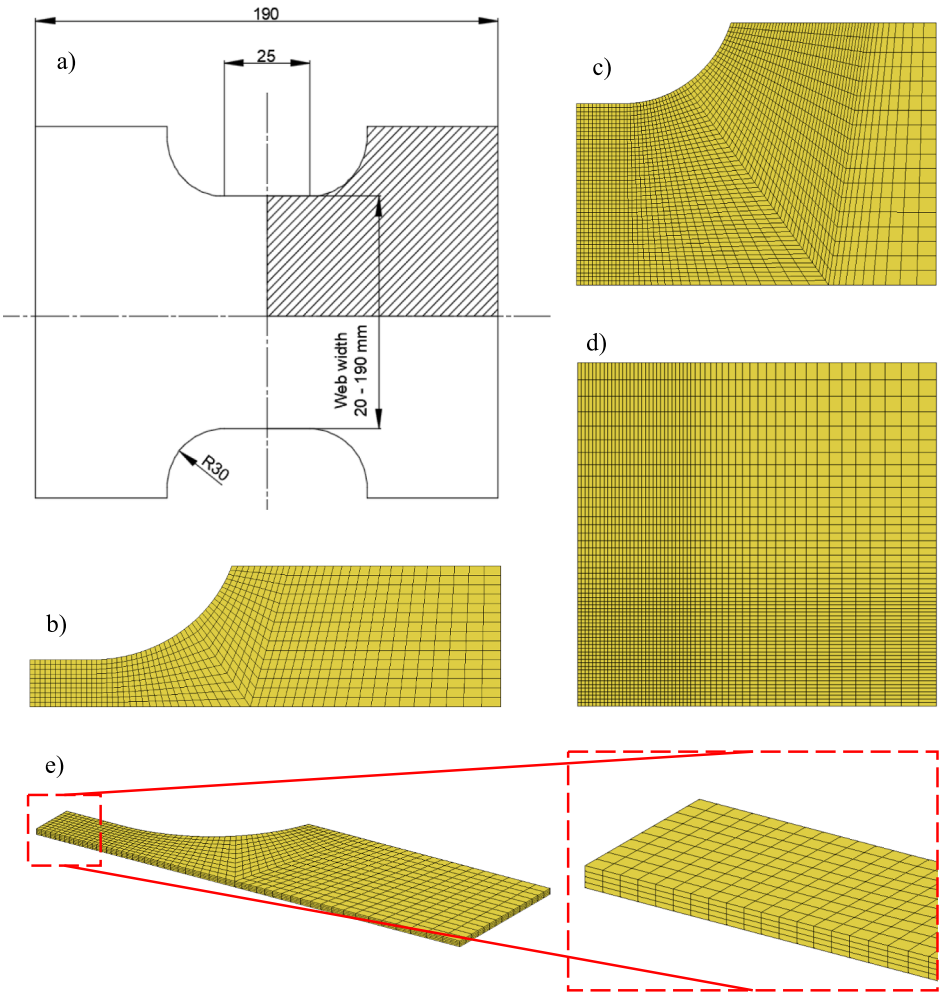

Fig. 22. A) a schematic view representing the dimensions of the nakajima test samples [66] and mesh layouts of b) w20, c) w90, d) w190, and e) elements through thickness.

fracture value for the combination of stress triaxiality and Lode parameter in the 2D fracture locus (Fig. 14) and 3D fracture locus (Figs. 15 and 16).

4. Results and discussion

This section explains the analytical predictions and numerical predictions of FLCs. Initially, the analytical predictions acquired by isotropic (Mises) and anisotropic (HomPol6) identification methodologies will be presented. Afterward, the numerical prediction results were compared with the analytical predictions. In addition, the strain paths were also acquired, and the overall results were discussed. The principal major plastic strains can be determined by following equations.

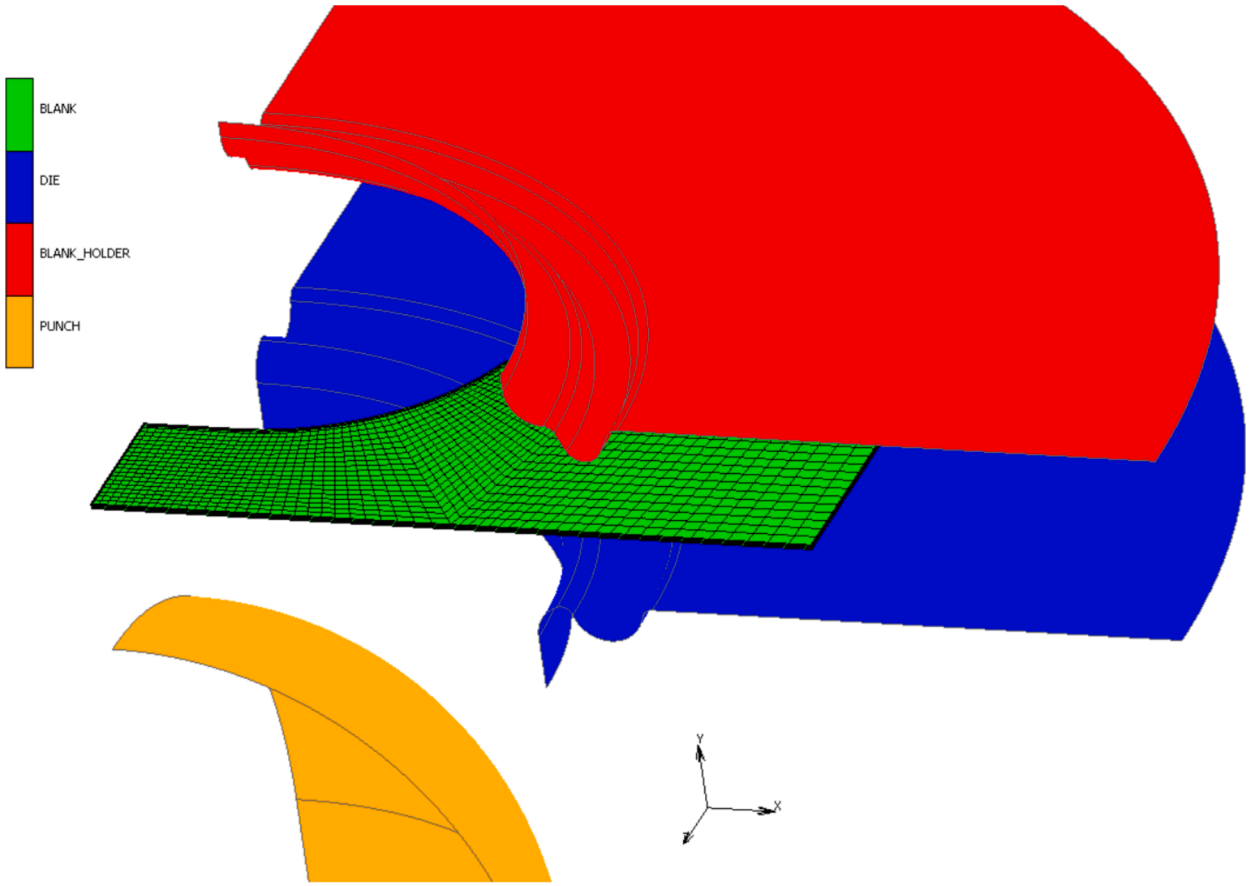

Fig. 23. FE model of the Nakajima test.

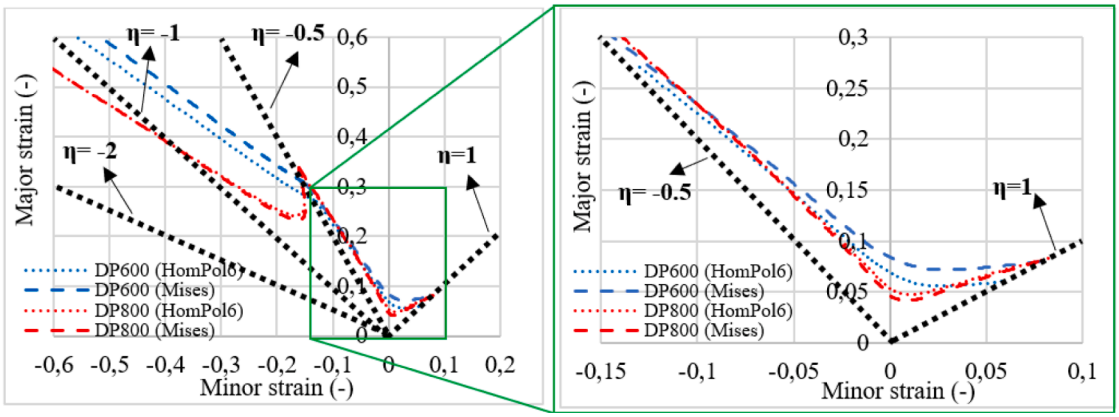

a) b)

Fig. 24. FLC curves predicted by analytical approaches with different calibration methodologies, a) wider spectrum, b) between the uniaxial tension and balanced biaxial tension lines.

$$d\varepsilon_1^p = d\varepsilon_{eq,f}^p\left(\frac{3-L}{2\sqrt{L^2+3}}\right) \quad (46)$$

$$d\varepsilon_2^p = d\varepsilon_{eq,f}^p\left(\frac{2L}{2\sqrt{L^2+3}}\right) \quad (47)$$

$$d\varepsilon_3^p = d\varepsilon_{eq,f}^p\left(\frac{-3-L}{2\sqrt{L^2+3}}\right) \quad (48)$$

The major total strains can be obtained by including the elastic strains in Eqs. (46)–(48). Accordingly, the analytical results of both isotropic and anisotropic identification methodologies are illustrated in Fig. 24.

The effect of identification methodology is more apparent in DP600 steel than the DP800. The predictions slightly deviated from each other, especially on the right side of the FLC (From the plane strain tension to the balanced biaxial tension state). Regarding the yield stress ratio directionalities (Fig. 5a and Fig. 6a) and the yield surfaces (Fig. 6), the anisotropic effect is more blatant for DP600 steel compared to DP800 steel. Moreover, the variations of the stress triaxiality and Lode parameter during the analyses of the tensile tests are more distinct for the DP600 steel. Correspondingly, the difference in isotropic and anisotropic identification methodologies turned out to be apparent for DP600 steel. For DP800 steel, a minor deviation was observed near the plane strain tension line. The analytical predictions emphasize the impact of the calibration methodology on fracture prediction. Recently, this outcome was also emphasized by Li et al. [57]. The FFLCs procured from the literature studies were compared with the of FFLCs obtained in this work for both steels and the comparisons are demonstrated in Fig. 25.

In the experimental acquisition of FFLC, there are position-based and visual based methodologies [71]. In the visual-based methodologies, the surface of the specimen is monitored through a high-resolution camera and the picture prior to the crack observation is regarded. The major and minor strains were measure through the pictures acquired from the high-resolution camera. As for the position-based methodologies, the two sides of the observable crack are regarded. A detailed explanation can be found in the literature [71]. Physical Nakajima test is an extensively utilized method for detecting the FFLC [10,71,75–77].

In this study, the thickness of the DP600 steel is much lower than the studies in the existing literature [7,40,78–82]. Moreover, it was also reported in the literature studies that the decrease in the thickness yields a decrease in the FLC [83,84]. In the comparison above, for both steels, the analytical predictions are consistent with the experimental and analytical outcomes from the literature for the left side of the FFLC. A similar situation can also be noticed for DP800 steel. The reason may be that the notched specimens curated in this study for calibrating the fracture model (CH, NT10, and NT20 specimens) correspond to the uniaxial tension and plane strain tension lines. Therefore, the left side is well-predicted for both steels. However, a discrepancy was observed for the right side of FFLC. The lower level of predicted FFLCs at the right side of the diagram for both DP steels can be explained by the material supplier, chemical decomposition, and low thickness value [7,74,85].

For DP600 steel, Hussein et al. [86] conducted a study regarding the crystal plasticity-based analytical Keeler-Brazier model using representative volume elements. On the other hand, Sarraf et al. [78], and Yu and Zheng [80] conducted studies including physical experiments with the DP600 steels of 1.48 mm and 1.2 mm thickness values. The predictions for DP600 steel obtained in this research are consistent with the experimental and analytical results from the literature for the left side of FFLC. The predictions showed that deviations for the right side of the FFLC may stem from the material supplier and the thickness of the material [7,80,85]. As for the DP800, the predictions in this research were consistent with the experimental data [87,88] near the uniaxial tension zone and toward the plane strain tension as well. Moreover, the predictions showed a similar slope and trend to the analytical predictions of Espinosa [89] on the right side of the FLC. The anisotropic calibration is slightly over the isotropic calibration results and more consistent with the experimental and analytical predictions from the literature studies. Nonetheless, a deviation is observed near the plane strain tension line. The deviation near the plane strain may result from the material supplier, the thickness of the material (The thickness of DP800 steels used for comparison [84–86] varies between 1 mm and 1.6 mm), and the chemical composition of the steel [7,80,85].

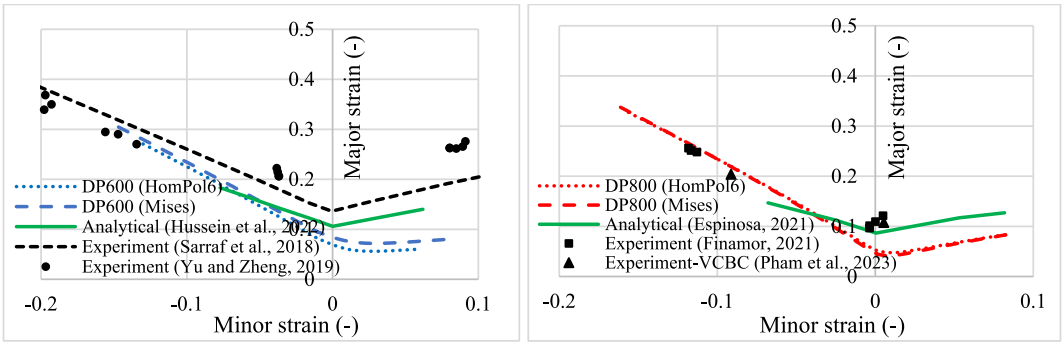

Fig. 25. Comparison of analytical and experimental FFLC predictions for a) DP600, b) DP800 steels.

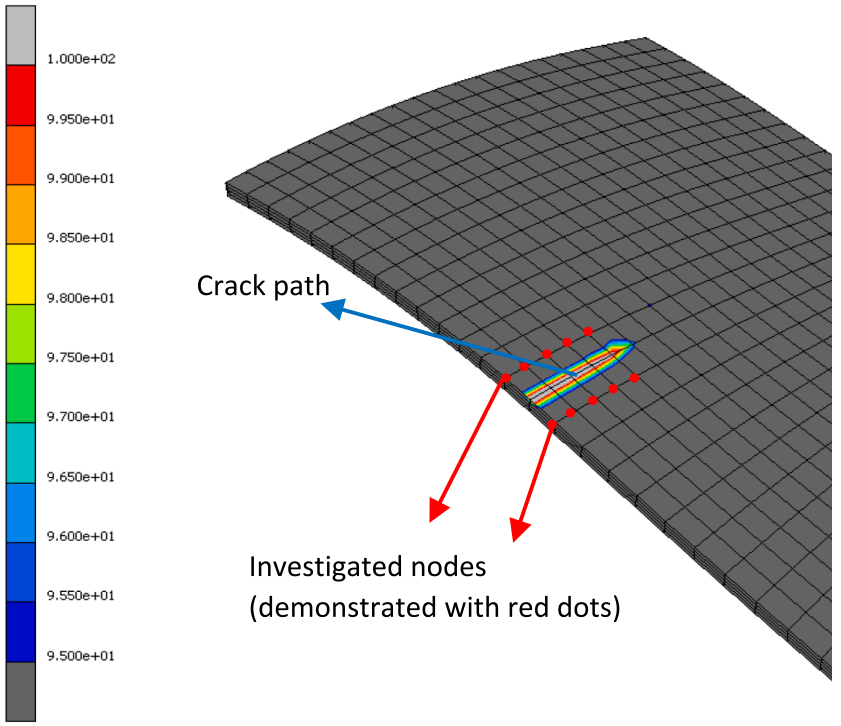

Fig. 26. The selected nodes for the specimen with 40 mm web width near the crack path.

4.1. Effect of numerical factors on the FFLC predictions with anisotropic identification approach

In the second stage, the calibrated parameters of the HomPol6 anisotropic yield criterion and DF2016 ductile fracture model were employed for the Hypela2 user-defined material subroutine for implementation into the Marc FE solver, and the numerical results were acquired from the Nakajima test simulations based on the identification and the sheet's anisotropy simultaneously.

The results were compared with the analytical results for reciprocal steel. To this end, the strain paths were attained from the Nakajima test simulations for each sample up to the crack initiation point. Afterward, a regression curve was generated representing all fracture initiation points. In Nakajima test simulations, the major and minor strains were acquired from the reciprocal two sides of the crack location at the increment in which the crack was observed. 8–10 nodes were selected from the two sides of the crack to determine the major and minor strains, and the average values for major and minor strains were calculated. The selection of nodes near the crack path is demonstrated in Fig. 26 for the specimen with a web width of 40 mm.

When a crack is observed in physical tests, major and minor strains cannot be measured from the crack side. Therefore, the nodes on

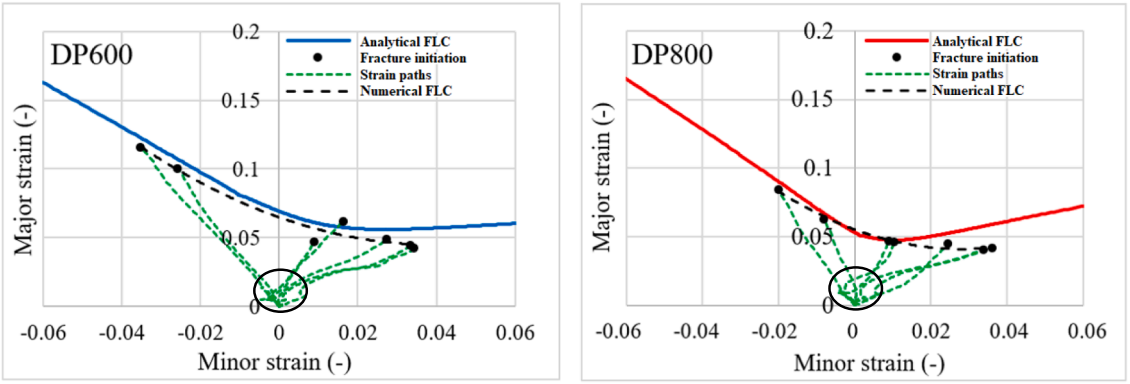

a) b)

Fig. 27. FLC curves predicted by analytical and numerical approaches for anisotropic calibration a) DP600, b) DP800.

the crack path were not considered directly for major and minor strain determination. The major and minor strains are measured based on visual-based and position-based methods in the literature [66]. In the position-based methods, the grids near the crack zone were considered. The major and minor strains were measured from these grids, or a correlation was established between the grids on the reciprocal sides of the crack zone. In order to reflect the physical experimental conditions of the numerical approach, the nodes near the crack paths were considered to be in line with the position-based methods. The strain paths were generated by applying a regression curve regarding the average value of the selected nodes ranging near the crack zone, and the strain paths were generated for each Nakajima sample up to the increment at which the crack was observed numerically. The comparative FLC predictions (numerical and analytical predictions) and strain paths for each Nakajima sample are demonstrated in Fig. 27.

In Fig. 27, the red and blue curves represent the analytical predictions of both steels, while the dashed black curves represent the numerical regression curve generated based on the fracture initiation strain for each sample. The green curves represent the strain paths obtained from the simulations of each sample. Since, Nakajima test covers from the uniaxial tension ($\eta = -0.5$) to the balanced biaxial tension ($\eta = 1$), Fig. 27 is generated throughout this region that is important for sheet metal forming. The average minor and major values of the nodes near the fracture initiation zone were determined. For both steels, the numerical curves were laid below the analytical predictions and tended to approach the vicinity of the plane strain tension line. The differences in strains are increased toward the balanced biaxial and uniaxial tension lines. Moreover, in the Nakajima test, the punch's displacement induced the strain paths, leading to the bending effect. The blank's contact surface interacting with the punch is exposed to compression due to bending. Therefore, the crack initiates on the reverse surface of the sample, where the biaxial tensile stresses occur due to bending. The combination of the biaxial tensile stresses due to bending and the corresponding stress and strain state due to sample geometry interacted together, and the strain paths varied. Moreover, the biaxial stress due to bending increases the stress triaxiality, which may reduce the fracture initiation strain [16,17,33–35]. Therefore, nonlinear strain paths emerged. These results showed that the combination of numerical factors such as friction, contact algorithm, draw a bead, element type, mesh layout, and the anisotropy of the Nakajima samples, crack detection-measurement method, bending through a punch, etc., influenced and decreased the FLC prediction.

4.2. *Effect of sheet's anisotropy on the FLC prediction*

This section evaluated the effect of the sheet's anisotropy in Nakajima simulations on the numerical FLC prediction. Since the anisotropic effect is more evident for DP600 steel, in this section, DP600 steel is regarded for assessing the sheet's anisotropy. To this end, the Nakajima test simulations were repeated, considering the DF2016 parameters acquired by the isotropic identification procedure. In Nakajima test simulations, the sheet's anisotropy was also disregarded, and blank is assumed to be isotropic. Fig. 28 illustrates the comparative results of DP600.

In Fig. 28, the major and minor strains were measured in the analysis results using a method identical to the previous section. As seen in Fig. 28a, the numerical FFLC prediction highly deviated from the analytical FFLC based on isotropic identification methodology, contrary to the anisotropic identification methodology. This outcome indicated that the isotropic assumption led to a significant discrepancy compared to the anisotropic identification. Analytical predictions generally lack strain variation at the crack zone and biaxial stress state due to bending, strain measuring techniques, and other numerical parameters. Hence, these findings may result from the numerical factors. As for the comparisons of both anisotropic and numerical predictions presented in Fig. 28b, regarding both the anisotropic identification methodology and sheet's anisotropy coupled with the other numerical factors mentioned above in Nakajima test simulations, the analytical and numerical results were coherent. However, this coherency was disrupted when the isotropic identification methodology was employed, and the sheet's anisotropy was disregarded. The numerical HomPol6 criterion's prediction was slightly lower than the analytical prediction of HomPol6, whereas a significant difference is observed for Mises criterion (Fig. 28b). This difference is resulting from the increase in stress triaxiality at the top side of the blank due to the bending effect (explained in the manuscript) leading to a decrease in FFLC. However, the HomPol6 provided more reliable prediction performance compared to the Mises criterion since the results are more consistent with each other. Moreover, the crack zone turned out to be

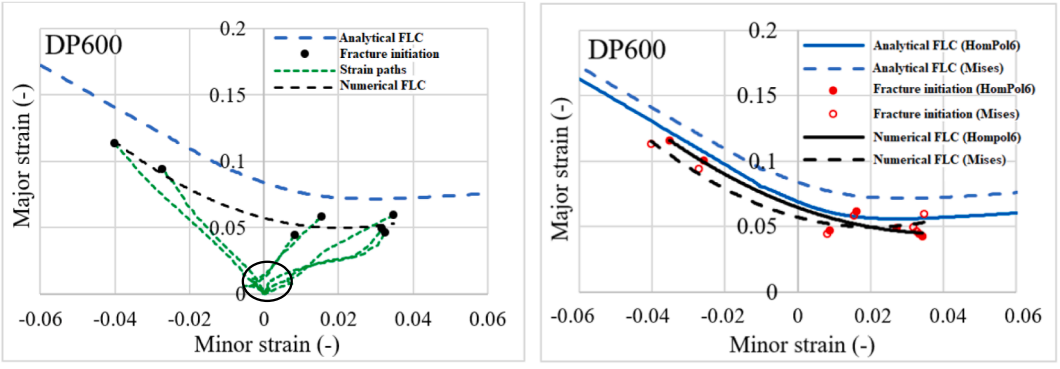

Fig. 28. FFLC curves predicted by analytical and numerical approaches for DP600 a) Isotropic calibration, b) Comparative results.

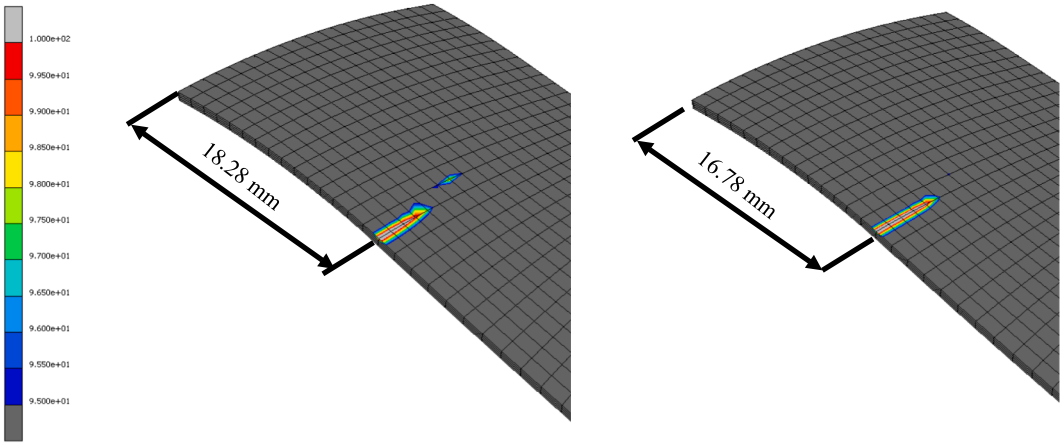

Fig. 29. Crack initiation zone of the specimen with the web width of 40 mm for a) anisotropic, b) isotropic identification methodologies (For anisotropic identification methodology, the crack initiated at the 15th node from the pole, while the crack initiated at the 14th node from the pole for the isotropic identification methodology).

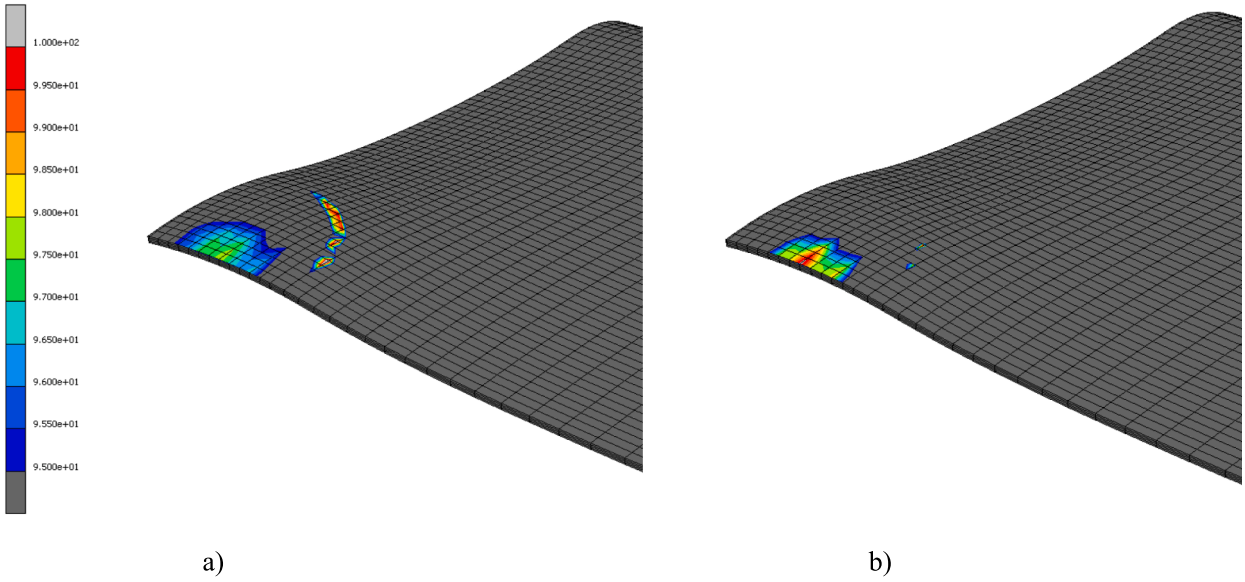

Fig. 30. Crack initiation zone of the specimen with the web width of 130 mm for a) anisotropic, b) isotropic identification methodologies.

different for the identical samples of the Nakajima test simulations when the sheet's anisotropy was taken into consideration. The fracture initiation zone was either shifted or noticeably changed. Besides, for the identical specimens, the fracture strokes correspondingly, the fracture strains were different with respect to both identification methodologies. Fig. 29 illustrates the crack initiation zones for both methodologies corresponding to the specimen with a 40 mm web width.

As seen in Fig. 29, the fracture initiation is closer to the pole for the isotropic identification methodology. The sheet's anisotropy shifted the crack zone. The change in the crack zone and the fracture stroke affected the fracture initiation strain as well. Fig. 30 demonstrates the change in the crack zone for the specimen with a web width of 130 mm.

The crack initiation zone was altered remarkably for specimens with the 130 mm web width. The difference in the numerical outcomes of FFLC was mainly a result of the sheet's anisotropy, which influenced the fracture initiation zone and, correspondingly, the minor-major strains. These results also pointed out that both anisotropic identification methodology and FE simulations of the Nakajima test regarding the sheet's anisotropy are significant.

5. Conclusion

This research delves into the difference in analytical and numerical predictions of an advanced ductile fracture model, specifically emphasizing isotropic and anisotropic calibration. DP600 and DP800 steels were employed as the test sheets. The DF2016 ductile fracture model, regarding both stress triaxiality and Lode parameters, was adopted in this regard. The HomPol6 criterion regarding the effects of Lankford's coefficients, yield stress ratios, and biaxial data simultaneously was also employed for yield locus representation. Both the HomPol6 yield criterion and DF2016 ductile fracture model were calibrated and incorporated into the Marc FE software by means of the Hypela2 user-defined material subroutine generated in the Fortran programming language. The standard uniaxial tensile test data were utilized to calibrate the hardening behavior and HomPol6 anisotropic yield criterion, while the notched uniaxial tensile test specimens were used to adjust the DF2016 ductile fracture criterion. Initially, the HomPol6 criterion was calibrated for DP600 and DP800 steels, and the FE simulations of notched tensile test specimens were conducted based on the Mises isotropic and HomPol6 anisotropic yield criteria, respectively. The results were compared with the experimental outcomes, and the DF2016 criterion was adjusted separately based on isotropic and anisotropic calibration methodologies. Correspondingly, the FFLCs were analytically predicted for both approaches. In the second stage, the FE analyses of the Nakajima test were carried out to acquire the numerical FFLCs considering the effect of the numerical parameters. Similarly, the analyses were performed based on isotropic Mises and anisotropic HomPol6 yield criteria separately to distinguish the impact of the sheet's anisotropy in a numerical approach. The conclusions are summarized as follows.

- Both DP steels demonstrated deformation-induced anisotropy. Besides, the r values and yield stress ratios, crucial as an indicator of thinning and tearing, are noticeably distributed for different orientations. The difference in distributions is more evident in r value orientation, which leads to significant anisotropic features of both DP steels. The HomPol6 criterion exhibited successful prediction accuracy for the anisotropic response of both DP steels.
- HomPol6 anisotropic yield criterion was successfully coupled with the DF2016 fracture model implemented in an implicit software (FE Marc software) having a Backward Euler stress update scheme in conjunction with the return mapping algorithm for the first time in the literature in order to predict the fracture prediction accurately.
- A distinct difference was observed between the analytical FFLC predictions of isotropic Mises and anisotropic HomPol6, especially for DP600 steel. The calibration methodology was found to be a prominent factor in the analytical approach. This situation underscoring that yield anisotropy cannot be neglected if accurate fracture-limit predictions are desired for advanced high-strength steels in automotive or similar forming applications. The evolution of the strain was highly affected by the material's anisotropy, which led to a noticeable difference in FFLC predictions.
- The analytical FFLC results were compared with the experimental results procured from the literature studies. It was observed that the analytical FFLC results were compatible with the experimental outcomes for the left side of the FFLC. Regarding the selected specimens with the notched geometries such as CH, NT10, and NT20 representing the high triaxiality region covering the uniaxial tension and plane strain tension lines, the validation of the FFLC with the experimental results was found to be highly dependent on the notched uniaxial tensile test specimen curation.
- The numerical FFLCs were also acquired from the FE simulations of the Nakajima test. In the first stage, the sheet's anisotropy was also taken into account by incorporating the HomPol6 criterion in the FE results. There were significant differences between the FE results and analytical FLCs (Employing the DF2016 parameters procured from the anisotropic calibration methodology) for both materials. The deviations were observed in the vicinity of uniaxial tension and balanced biaxial tension states, especially for DP600 steel. Nakajima simulations indicate that the numerical factors (friction, contact algorithm, draw bead, element type, mesh layout, and the anisotropy of the Nakajima samples, bending through a punch) reduce the FFLC relative to an analytical approach. Among these numerical factors, the bending effect led to an additional biaxial tensional stress at the reverse side of the sheet, and the biaxial tension state increased the triaxiality. Noting that the increase in triaxiality has an adverse effect on the equivalent plastic fracture strain, the increase in triaxiality due to the incorporation of the biaxial stress into the corresponding stress state triggered by the web-width geometry of the Nakajima samples at the reverse side of the sheet which might decrease the fracture initiation strain.
- In the previous step, the Nakajima test simulations were conducted by considering the sheet's anisotropy to assess the numerical and analytical approaches using the parameters obtained from the anisotropic calibration procedure. In the second stage of the study, in order to set forth the sheet's anisotropy's effect on FE predictions of FFLC, the FE simulations of the Nakajima test were repeated by disregarding the sheet's anisotropy, and the results were compared. It was seen that the difference between the analytical predictions and the numerical predictions of FFLC was significantly increased for the isotropic calibration methodology. These results showed that the sheet's anisotropy is one of the prominent factors. The fracture initiation zones and, correspondingly, the fracture strains for Nakajima test samples were different, for the sheet's anisotropy was regarded and disregarded. Although in most of the research in the literature, the isotropic yield criterion was utilized for the sake simplicity [40–42,47,49–51], the difference between the analytical and numerical results were noticeably high when compared to the anisotropic approach.
- Future studies should examine how anisotropic ductility itself influences fracture outcomes, potentially requiring a fully anisotropic fracture criterion. While the DF2016 fracture law used here is isotropic, our findings imply that fully anisotropic fracture behavior could be relevant for strongly textured steels. Future experiments regarding the oriented notched tensile specimens at 0°, 45°, and 90° may be required to capture the full directional dependence of fracture ductility, offering a path toward anisotropic fracture criteria in the spirit of references [68,69].

In summary, it was seen that the fracture strain is affected by the sheet's anisotropy from different perspectives. The material's anisotropy is essential in both the calibration of the ductile fracture model and the Nakajima test simulations. Either for simplicity or the computational and implementational difficulties, disregarding the material's anisotropy leads to unreliable FFLC results. Moreover, for a reliable FFLC prediction, the physical test conditions should be taken into account. Noting that in most of the formability tests and processes, including the Nakajima test, bending is the dominant factor affecting the stress state through the thickness, and the analytical predictions of FFLC may lead to significant drawbacks. The stress states for each sample of the Nakajima test were dramatically affected by the incorporation of the biaxial tension at the reverse side of the sheet due to the bending. In addition to the bending effect, the effects of the element type, friction-lubrication condition, and the geometry of the die tools are disregarded in the analytical FFLC predictions. Numerical approaches should be implemented in order to enhance the reliability of the FFLC predictions. Furthermore, this work highlights the significance of accurate yield modeling when calibrating ductile fracture laws for DP steels. Anisotropic yield surfaces (like HomPol6) capture essential directional effects on stress states, thereby altering the predicted fracture onset. Although a fully anisotropic fracture model remains beyond the current scope, these results establish a critical step: even an "isotropic" fracture criterion behaves differently when coupled with anisotropic plasticity. Accounting for this interplay will enhance reliability in forming simulations, guiding future research toward unified, anisotropic constitutive and fracture frameworks for high-performance steels.

CRediT authorship contribution statement

Toros Arda Akşen: Writing – original draft, Software, Formal analysis, Data curation. **Neslihan Özsoy:** Writing – original draft, Validation. **Emre Esener:** Writing – review & editing, Methodology, Data curation. **Murat Özsoy:** Visualization, Conceptualization. **Mehmet Fırat:** Supervision, Methodology, Conceptualization.

Declaration of competing interest

The authors declare the following financial interests/personal relationships which may be considered as potential competing interests: [Mehmet FIRAT reports financial support was provided by Sakarya University. If there are other authors, they declare that they have no known competing financial interests or personal relationships that could have appeared to influence the work reported in this paper].

Acknowledgements

This research was supported by the Sakarya University Scientific Research Projects Unit under project number of 2022-9-32-76. The authors would like to thank the Sakarya University Scientific Research Projects Unit for providing the financial support.

Data availability

No data was used for the research described in the article.

References

[1] W. Wang, X. Wei, The effect of martensite volume and distribution on shear fracture propagation of 600–1000 MPa dual phase sheet steels in the process of deep drawing, Int. J. Mech. Sci. 67 (2023) 100–107, https://doi.org/10.1016/j.ijmecsci.2012.12.011.
[2] A. Alaie, J. Kadkhodapour, S.Z. Rad, M.A. Asadabad, S. Schmauder, Formation and coalescence of strain localizedregions in ferrite phase of DP600 steels under uniaxial tensile deformation, Mater. Sci. Eng. A 623 (2015) 133–144, https://doi.org/10.1016/j.msea.2014.11.042.
[3] E.E. Aşık, E.S. Perdahcıoğlu, A.H. van den Boogaard, Microscopic investigation of damage mechanisms and anisotropic evolution of damage in DP600,", Mater. Sci. Eng. A 739 (2019) 348–356, https://doi.org/10.1016/j.msea.2018.10.018.
[4] J. Lian, A method to quantitatively upscale the damage initiation of dual-phase steels under various stress states from microscale to macroscale, Comput. Mater. Sci. 94 (2014) 245–247, https://doi.org/10.1016/j.commatsci.2014.05.051.
[5] A. Fillafer, C. Krempaszky, E. Werner, On strain partitioning and micro-damage behavior of dual-phase steels, Mater. Sci. Eng. A 614 (2014) 180–192, https://doi.org/10.1016/j.msea.2014.07.029.
[6] F.X.C. Andrade, M. Feucht, A. Haufe, F. Neukamm, An incremental stress state dependent damage model for ductile failure prediction, Int. J. Fract. 200 (2016) 127–150, https://doi.org/10.1007/s10704-016-0081-2.
[7] S. Qin, Y. Lu, S.B. Sinnott, A.M. Beese, Influence of phase and interface properties on the stress state dependent fracture initiation behavior in DP steels through computational modeling, Mater. Sci. Eng. A 776 (2020) 138981, https://doi.org/10.1016/j.msea.2020.138981.
[8] R. Hill, On discontinuous plastic states, with special reference to localized necking in thin sheets, J. Mech. Phys. Solids. 1 (1952) 19–30, https://doi.org/10.1016/0022-5096(52)90003-3.
[9] Z. Marciniak, K. Kuczynski, Limit strains in the processes of stretch-forming sheet metal, Int. J. Mech. Sci. 9 (1967) 609–620, https://doi.org/10.1016/0020-7403(67)90066-5.
[10] Y. Lou, J.W. Yoon, Anisotropic ductile fracture criterion based on linear transformation, Int. J. Plast. 93 (2017) 3–25, https://doi.org/10.1016/j.ijplas.2017.04.008.
[11] C. Cheng, B. Meng, J.Q. Han, M. Wan, X.D. Wu, R. Zhao, A modified Lou-Huh model for characterization of ductile fracture of DP590 sheet, Mater. Des. 118 (2017) 89–98, https://doi.org/10.1016/j.matdes.2017.01.030.
[12] T. Xu, F. Li, X. Wang, G. Zhang, Modeling anisotropic ductile fracture of AA7075-T6 sheet for sheet metal forming considering anisotropic stress state, Theor. Appl. Fract. Mech. 122 (2022) 103610, https://doi.org/10.1016/j.tafmec.2022.103610.
[13] T.J. Grillo, R.A.F. Valente, R.J. Alves de Souza, Modelling non-quadratic anisotropic yield criteria and mixed isotropic-nonlinear kinematic hardening: analysis of forward and backward-Euler formulations, Int. J. Mater. Form. 8 (2015) 533–547, https://doi.org/10.1007/s12289-014-1176-9.

[14] M. Halilovic, M. Vrh, S. Boris, NICE-An explicit numerical scheme for efficient integration of nonlinear constitutive equations, Math. Comput. Simul. 80 (2009) 294–313, https://doi.org/10.1016/j.matcom.2009.06.030.
[15] M. Halilovic, B. Starman, M. Vrh, S. Boris, A robust explicit integration of elasto-plastic constitutive models, based on simple sub increment size estimation, Eng. Comput. 34 (6) (2017) 1774–1806, https://doi.org/10.1108/EC-03-2016-0103.
[16] Y. Li, M. Luo, J. Gerlach, T. Wierzbicki, Prediction of shear-induced fracture in sheet metal forming, J. Mater. Process. Technol. 201 (2010) 1858–1869, https://doi.org/10.1016/j.jmatprotec.2010.06.021.
[17] N.M. Mekonen, D. Steglich, J. Bohlen, L. Stutz, D. Letzig, J. Mosler, Experimental and numerical investigation of Mg alloy sheet forming, Mater. Sci. Eng. A 586 (2013) 204–214, https://doi.org/10.1016/j.msea.2013.07.088.
[18] T.A. Akşen, B. Sener, M. Firat, Failure prediction capability of generalized plastic work criterion, Proced. Manuf. 47 (2020) 1235–1240, https://doi.org/10.1016/j.promfg.2020.04.190.
[19] F. Ozturk, S. Toros, S. Kılıç, Effect of anisotropic yield functions on prediction of forming limit diagrams of DP600 advanced high strength steels, Proc. Eng. 81 (2014) 760–765, https://doi.org/10.1016/j.proeng.2014.10.073.
[20] A. Singh, S. Basak, L. Prakash, G.G. Roy, M.N. Jha, M. Mascarenhas, S.K. Panda, Prediction of earing defect and deep drawing behavior of commercially pure titanium sheets using CPB06 anisotropy yield theory, J. Manuf. Process. 33 (2018) 256–267, https://doi.org/10.1016/j.jmapro.2018.05.003.
[21] R. Hill, A theory of the yielding and plastic fow of anisotropic metals, Proc. r. Soc. A Math. Phys. Eng. Sci. 193 (1948) 281–297, https://doi.org/10.1098/rspa.1948.0045.
[22] K. Chung, N. Ma, T. Park, D. Kim, D. Yoo, C. Kim, A modified damage model for advanced high strength steel sheets, Int. J. Plast. 27 (2011) 1485–1511, https://doi.org/10.1016/j.ijplas.2011.01.007.
[23] J. Woodthrope, R. Pearce, The anomalous behavior of aluminum sheet under balanced biaxial tension, Int. J. Mech. Sci. 12 (1970) 341–347, https://doi.org/10.1016/0020-7403(70)90087-1.
[24] M. Gotoh, A theory of plastic anisotropy based on a yield function of fourth order (plane stress state)– I, Int. J. Mech. Sci. 19 (9) (1977) 505–512, https://doi.org/10.1016/0020-7403(77)90043-1.
[25] D. Banabic, Sheet Metal Forming Processes Constitutive Modelling, and Numerical Simulation, first ed., Heidelberg, Berlin, 2010.
[26] F. Barlat, J.C. Brem, J.W. Yoon, K. Chung, R.E. Dick, D.J. Lege, F. Pourboghrat, S.H. Choi, E. Chu, Plane stress yield function for aluminum alloy sheets—part 1: theory, Int. J. Plast. 19 (9) (2003) 1297–1319, https://doi.org/10.1016/S0749-6419(02)00019-0.
[27] F. Barlat, H. Aretz, J.W. Yoon, M.E. Karabin, J.C. Brem, R.E. Dick, Linear transfomation-based anisotropic yield functions, Int. J. Plast. 21 (2005) 1009–1039, https://doi.org/10.1016/j.ijplas.2004.06.004.
[28] S. Soare, J.W. Yoon, O. Cazacu, On the use of homogeneous polynomials to develop anisotropic yield functions with applications to sheet forming, Int. J. Plast. 24 (2018) 915–944, https://doi.org/10.1016/j.ijplas.2007.07.016.
[29] S.C. Soare, M. Diehl, Calibration and fast evaluation algorithms for homogeneous orthotropic polynomial yield functions, Comput. Mech. 73 (2024) 1219–1239, https://doi.org/10.1007/s00466-023-02408-6.
[30] M. Oyane, Criteria of ductile fracture strain, Bull. JSME 15 (1972) 1507–1513, https://doi.org/10.1299/jsme1958.15.1507.
[31] L. Xue, Ductile fracture modeling – theory, experimental investigation and numerical verification, PhD. Thesis, Department of Mechanical Engineering, Massachusetts, USA, 2007.
[32] Y. Bai, Effect of loading history on necking and fracture, Ph.D. Thesis, Department of Mechanical Engineering, Massachusetts, USA, 2008.
[33] F.A. McClintock, A criterion of ductile fracture by growth of holes, J. Appl. Mech. 35 (1968) 363–371, https://doi.org/10.1115/1.3601204.
[34] M.G. Cockcroft, D.J. Latham, Ductility and the workability of metals, J. Inst. Met. 96 (1968) 33–39.
[35] J.R. Rice, D.M. Tracey, On the ductile enlargement of voids in triaxial stress fields, J. Mech. Phys. Solids. 17 (1969) 201–217, https://doi.org/10.1016/0022-5096(69)90033-7.
[36] Y., Bao, (2003), Prediction of ductile crack formation in uncracked bodies, Ph.D. Thesis, Department of Mechanical Engineering, Massachusetts, USA.
[37] A.L. Gurson, Continuum theory of ductile rupture by void nucleation and growth. Part I: yield criteria and flow rules for porous ductile media, J. Eng. Mater. Technol. 99 (1977) 2–15, https://doi.org/10.2172/7351470.
[38] V. Tvergaard, A. Needleman, Analysis of the cup-cone fracture in a round tensile bar, Acta Metall. 32 (1984) 159–169, https://doi.org/10.1016/0001-6160(84)90213-X.
[39] J. Lemaitre, A continuous damage mechanics model for ductile fracture, J. Eng. Mater. Technol. 107 (1985) 83–89, https://doi.org/10.1115/1.3225775.
[40] N. Habibi, A. Ramazani, V. Sundararaghavan, U. Prahl, Failure predictions of DP600 steel sheets using various uncoupled fracture criteria, Eng. Fract. Mech. 190 (2018) 367–381, https://doi.org/10.1016/j.engfracmech.2017.12.022.
[41] S.J. Park, K. Lee, B.C. Cerik, J. Choung, Comparative study on various ductile fracture models for marine structural steel EH36, J. Ocean Eng. Technol. 33 (2019) 259–271, https://doi.org/10.26748/KSOE.2019.038.
[42] S.J. Park, B.C. Cerik, J. Choung, Comparative study on ductile fracture prediction of high-tensile strength marine structural steels, Ships and Offshore Struct. 15 (2020) 1–12, https://doi.org/10.1080/17445302.2020.1743552.
[43] Y. Bai, T. Wierzbicki, Application of extended Mohr-Coulomb criterion to ductile fracture, Int. J. Fract. 161 (2010) 1, https://doi.org/10.1007/s10704-009-9422-8.
[44] Y. Lou, Y. Huh, Prediction of ductile fracture for advanced high strength steel with a new criterion: experiments and simulation, J. Mater. Process. Technol. 213 (2013) 1284–1302, https://doi.org/10.1016/j.jmatprotec.2013.03.001.
[45] D. Mohr, S. Marcadet, Micromechanically motivated phenomenological Hosford-Coulomb model for predicting ductile fracture initiation at low stress triaxialities, Int. J. Solids Struct. 67–68 (2015) 40–55, https://doi.org/10.1016/j.ijsolstr.2015.02.024.
[46] Y. Lou, L. Chen, T. Clausmeyer, T. Tekkaya, A.E. Yoon, Modeling of ductile fracture from shear to balanced biaxial biaxial tension for sheet metals, Int. J. Solids Struct. 112 (2017) 169–184, https://doi.org/10.1016/j.ijsolstr.2016.11.034.
[47] D.Y. Kong, L.M. Ren, B. Yang, X.H. Zhou, M. Elchalakani, Comparative study of uncoupled ductile-fracture models on fracture prediction of structural steels under monotonic loading, J. Eng. Mech. 146 (2020) 1–18, https://doi.org/10.1061/(ASCE)EM.1943-7889.0001807.
[48] C.F. Kusche, F. Pütz, S. Münstermann, T. Al-Samman, S.K. Kerzel, On the effect of strain and triaxiality on void evolution in a heterogeneous microstructure – A statistical and single void study of damage in DP800 steel, Mater. Sci. Eng. A 799 (2021) 140332, https://doi.org/10.1016/j.msea.2020.140332.
[49] H. Ding, T. Zhu, X. Wang, B. Yang, S. Xiao, G. Yang, An uncoupled ductile fracture model considering void shape change and necking coalescence, Eng. Frac. Mech. 292 (2023) 109612, https://doi.org/10.1016/j.engfracmech.2023.109612.
[50] S.J. Park, K. Lee, W. Nam, K. Kim, B. Park, Numerical study on a ductile fracture model in pre-cracked tension tests of SUS304L, Mater. 17 (2024) 276, https://doi.org/10.3390/ma17020276.
[51] L. Zheng, Z. Wang, B. Meng, M. Wan, A unified ductile fracture criterion suitable for sheet and bulk metals considering multiple void deformation modes, Int. J. Plast. 164 (2023) 103574, https://doi.org/10.1016/j.ijplas.2023.103572.
[52] A. Kacem, H. Laurent, S. Thuillier, Experimental and numerical investigation of ductile fracture for AA6061-T6 sheets at room and elevated temperatures, Int. J. Mech. Sci. 222 (2022) 107201, https://doi.org/10.1016/j.ijmecsci.2022.107201.
[53] S. Zhang, Y. Lu, Z. Shen, C. Zhou, Y. Lou, Prediction of ductile fracture for Al6016-T4 with a ductile fracture criterion: experiment and simulation, Int. J. Damage Mech. 29 (2019) 1–23, https://doi.org/10.1177/1056789519865771.
[54] F. Barlat, D.J. Lege, J.C. Brem, A six-component yield function for anisotropic materials, Int. J. Plast. 7 (1991) 693–712, https://doi.org/10.1016/0749-6419(91)90052-Z.
[55] K. Wang, L. Meng, T. Wierzbicki, Experiments and modeling of Edge Fracture for an AHSS sheet, Int. J. Fract. 187 (2) (2014) 245–268, https://doi.org/10.1007/s10704-014-9937-5.
[56] V.K. Barnwal, S.Y. Lee, S.Y. Yoon, J.H. Kim, F. Barlat, Fracture characteristics of advanced high strength steels during hole expansion test, Int. J. Fract. 224 (2020) 217–233, https://doi.org/10.1007/s10704-020-00458-y.

[57] Z. Li, Y. Chang, W. Liu, J. Lian, Predicting edge fracture in dual-phase steels: significance of anisotropy-induced localization, Int. J. Mech. Sci. 274 (2024) 109255, https://doi.org/10.1016/j.ijmecsci.2024.109255.
[58] R. Li, Z. Zheng, M. Zhan, H. Zhang, Y. Lei, A comparative study of three forms of an uncoupled damage model as fracture judgment for thin-walled metal sheets, Thin Walled Struct. 169 (2021) 108321, https://doi.org/10.1016/j.tws.2021.108321.
[59] T. Akşen, B. Şener, E. Esener, M. Firat, Evaluation of ductile fracture criteria in combination with a homogenous polynomial yield function for edge splitting damage of DP steels, Mater. Test. 65 (6) (2023) 824–843, https://doi.org/10.1515/mt-2022-0359.
[60] ASTME517-19 Standard Test Method for Plastic Strain Ratio r for Sheet Metal. doi: 10.1520/E0517-19.
[61] S.C. Soare, On the use of homogeneous polynomials to develop anisotropic yield functions with applications to sheet forming. PhD Thesis, Department of Mechanical and Aerospace Engineering, Florida, USA, 2007.
[62] T.A. Akşen, M. Firat, Effect of the yield surface evolution on the earing defect prediction, Rev. Metall. 59 (1) (2023) e235.
[63] Y. Lou, Y. Huh, S. Lim, K. Pack, New ductile fracture criterion for prediction of fracture forming limit diagrams of sheet metals, Int. J. Solids & Struct. 49 (2012) 3605–3615, https://doi.org/10.1016/j.ijsolstr.2012.02.016.
[64] Y. Lou, J.W. Yoon, H. Huh, Modeling of shear ductile fracture considering a changeable cut-off value for the stress triaxiality, Int. J. Plast. 54 (2014) 56–80, https://doi.org/10.1016/j.ijplas.2013.08.006.
[65] R. Li, Z. Zheng, M. Zhan, H. Zhang, X. Cui, Y. Lei, Fracture prediction for metal sheet deformation under different stress states with uncoupled ductile fracture criteria, J. Manuf. Process. 73 (2022) 531–543, https://doi.org/10.1016/j.jmapro.2021.11.023.
[66] A.M. Beese, M. Luo, Y. Li, Y. Bai, T. Wierzbicki, Partially coupled anisotropic fracture model for aluminum sheets, Eng. Fract. Mech. 77 (2010) 1128–1152, https://doi.org/10.1016/j.engfracmech.2010.02.024.
[67] Z. Li, F. Shen, Y. Liu, C. Hartmann, R. Norz, S. Münstermann, W. Volk, J. Min, J. Lian, Anisotropic fracture behavior of the 3rd generation advanced high-strength – Quenching and Partitioning steels: experiments and simulation, J. Mater. Res. Technol. 30 (2024) 9395–9414, https://doi.org/10.1016/j.jmrt.2024.05.228.
[68] M. Luo, M. Dunand, D. Mohr, Experiments and modeling of anisotropic aluminum extrusions under multi-axial loading – Part II: ductile fracture, Int. J. Plast. 32–33 (2012) 36–58, https://doi.org/10.1016/j.ijplas.2011.11.001.
[69] G. Gu, D. Mohr, Anisotropic Hosford–Coulomb fracture initiation model: theory and application, Eng. Fract. Mech. 147 (2015) 480–497, https://doi.org/10.1016/j.engfracmech.2015.08.004.
[70] J. Ha, M. Baral, Y.P. Korkosis, Plastic anisotropy and ductile fracture of bake-hardened AA6013 aluminum sheet, Int. J. Solids Struct. 155 (2018) 123–139, https://doi.org/10.1016/j.ijsolstr.2018.07.015.
[71] R. Uppaluri, D. Helm, A convex fourth order yield function for orthotropic metal plasticity, Eur. J. Mech. / A Solids 87 (2021) 104196, https://doi.org/10.1016/j.euromechsol.2020.104196.
[72] J., Lian, A generalized hybrid damage mechanics model for steel sheets and heavy plates. PhD Thesis, Von der Fakultät für Georessourcen und Materialtechnik der Rheinisch-Westfälischen Technischen Hochschule Aachen, Aachen, Germany, 2015.
[73] Marc (2021), Volume A Theory and User Information. https://simcompanion.hexagon.com/customers/s/article/msc-marc-volume-a–theory-and-user-information-doc9245/Adobe PDFDOC9245 | vola.pdf, 20.05.2024.
[74] Marc (2012), Volume B Element Library. https://simcompanion.hexagon.com/customers/s/article/marc-2012-volume-b–element-library–doc10192/Adobe PDFDOC10192|marc_2012_doc_volume_b.pdf, 20.05.2024.
[75] J.A.L. Fernandez, M. Borrego, G. Centeno, C. Vallellano, Int. J. Mechanical Sci. 278 (2024) 109438, https://doi.org/10.1016/j.ijmecsci.2024.109438.
[76] S.A. Dizaji, H. Darendeliler, B. Kaftanoğlu, Prediction of forming limit curve at fracture for sheet metal using new ductile fracture criterion, European J. Mechanics / A Solids. 69 (2018) 255–265, https://doi.org/10.1016/j.euromechsol.2018.01.003.
[77] L.M. Valente Tigrinho, R.A. Chemin Filho, P.V. Prestes Marcondes, Fracture analysis approach of DP600 steel when subjected to different stress/strain states during deformation, Int. J. Adv. Manuf. Technol. 69 (2013) 1017–1024, https://doi.org/10.1007/s00170-013-5104-9.
[78] I.S. Sarraf, D.E. Green, D.M. Vasilescu, Y. Song, Numerical analysis of damage evolution and formability of DP600 sheet with am extended Rousselier damage model, Int. J. Solids Struct. 134 (2018) 70–88, https://doi.org/10.1016/j.ijsolstr.2017.10.030.
[79] K. Drotleff, M. Liewald, Application of and advanced necking criterion for nonlinear strain paths to a complex sheet metal forming component, IOP Conf. Ser.: Mater. Sci. Eng. 418 (2018) 012041, https://doi.org/10.1088/1757-899X/418/1/012041.
[80] H. Yu, Q. Zheng, Forming limit diagram of DP600 steel sheets during electrohydraulic forming, Int. J. Adv. Manuf. Technol. 104 (2019) 743–756, https://doi.org/10.1007/s00170-019-03885-x.
[81] J. Cheng, D.E. Green, S.F. Golovashchenko, Formability enhancement of DP600 steel sheets in electro-hydraulic die forming, J. Mater. Process. Techol. 344 (2017) 177–189, https://doi.org/10.1016/j.jmatprotec.2017.01.027.
[82] C. Maris, A. Hassannejadasl, D.E. Green, J. Cjeng, S.F. Golovashchenko, A.J. Gillard, Y. Liang, Comparison of quasi-sttic and electrohydraulic free forming limits for DP600 and AA5182 sheets, J. Mater. Process. Techol. 235 (2016) 206–219, https://doi.org/10.1016/j.jmatprotec.2016.04.028.
[83] M. Dilmec, H.S. Halkaci, F. Ozturk, H. Livatyali, O. Yigit, Effects of sheet thickness and anisotropy on forming limit curves of AA2024-T4, Int. J. Adv. Manuf. Technol. 67 (2013) 2689–2700, https://doi.org/10.1007/s00170-012-4684-0.
[84] W.J. Chen, H.W. Song, S.F. Chen, Y. Xu, S.Y. Deng, Z. Cai, X.H. Pei, S.H. Zhang, A new phenomenological model to predict forming limit curves from tensile properties for hot-rolled steel sheets, Metals 14 (2024) 168, https://doi.org/10.3390/met14020168.
[85] K. Prasad, D. Kumar, H. Krishnaswamy, D.K. Banerjee, Uncertainties in the Swift hardening law parameters and their influence on the flow stress and the hole expansion behavior of Dual-Phase (DP600) steel specimens, J. Mater. Eng. Perform. 32 (2023) 9206–9220, https://doi.org/10.1007/s11665-022-07793-2.
[86] T. Hussein, M. Umar, F. Qayyum, S. Guk, U. Prahl, Micromechanical effect of martensite attributes on forming limits of dual-phase steels investigated by crystal plasticity-based numerical simulations, Cryst. 12 (2022) 155, https://doi.org/10.3390/cryst12020155.
[87] Q.T. Pham, M.S. Islam, A. Barlo, M. Sigvant, An evaluation method for experimental necking detection of automotive sheet metals, IOP Conf. Ser.: Mater. Sci. Eng. 1284 (2023) 012020, https://doi.org/10.1088/1757-899X/1284/1/012020.
[88] F.P. Finamor, M.A. Wolff, V.S. Lage, Prediction of forming limit diagrams from tensile tests of automotive grade steels by a machine learning approach, IOP Conf. Ser.: Mater. Sci. Eng. 1157 (2021) 012080, https://doi.org/10.1088/1757-899X/1157/1/012080.
[89] Espinosa, E., (2021) Deformation response and formability limit diagram estimates of Dual-Phase steels. Thesis, The University of Guelph, Canada.